AD-A088 526 DAVID W TAYLOR NAVAL SHIP RESEARCH AND DEVELOPMENT CE--ETC F/G 20/4
BOUNDARY-LAYER FLOW ON AN AXISYMMETRIC BODY WITH AN INFLECTED S--ETC(U)
AUG 80 T T HUANG, N C GROVES, G BELT

UNCLASSIFIED DTNSRDC-80/064 NL

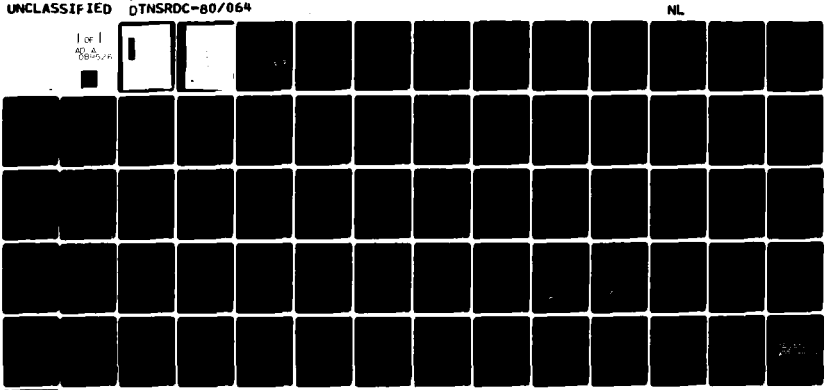

END
DATE FILMED
8-80
DTIC

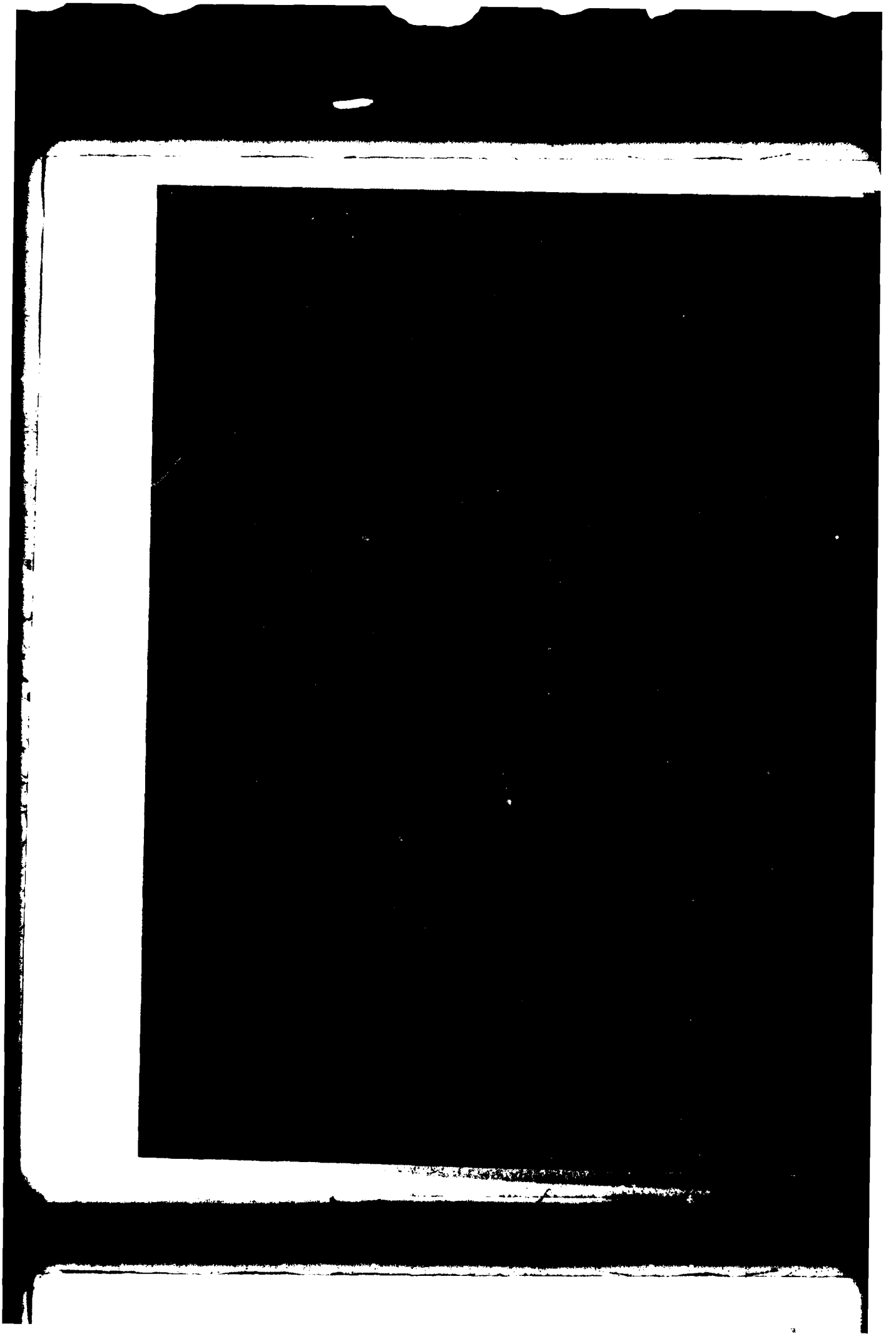

UNCLASSIFIED

SECURITY CLASSIFICATION OF THIS PAGE (When Data Entered)

REPORT DOCUMENTATION PAGE	READ INSTRUCTIONS BEFORE COMPLETING FORM
1. REPORT NUMBER: DTNSRDC-80/064 (14) 2. GOVT ACCESSION NO.: AD-A088526	3. RECIPIENT'S CATALOG NUMBER
4. TITLE (and Subtitle): BOUNDARY-LAYER FLOW ON AN AXISYMMETRIC BODY WITH AN INFLECTED STERN (6)	5. TYPE OF REPORT & PERIOD COVERED: Final
	6. PERFORMING ORG. REPORT NUMBER
7. AUTHOR(s): Thomas T. Huang / Nancy C. Groves / Garnell Belt (10)	8. CONTRACT OR GRANT NUMBER(s)
9. PERFORMING ORGANIZATION NAME AND ADDRESS: David W. Taylor Naval Ship Research and Development Center, Bethesda, Maryland 20084 (16)	10. PROGRAM ELEMENT, PROJECT, TASK AREA & WORK UNIT NUMBERS: Program Element 61152N; Project ZR 000 01; Work Unit 1552-103
11. CONTROLLING OFFICE NAME AND ADDRESS: (12) 70 (11)	12. REPORT DATE: Aug [redacted]80
	13. NUMBER OF PAGES: 66
14. MONITORING AGENCY NAME & ADDRESS (if different from Controlling Office)	15. SECURITY CLASS. (of this report): UNCLASSIFIED
	15a. DECLASSIFICATION/DOWNGRADING SCHEDULE

16. DISTRIBUTION STATEMENT (of this Report)

APPROVED FOR PUBLIC RELEASE: DISTRIBUTION UNLIMITED

17. DISTRIBUTION STATEMENT (of the abstract entered in Block 20, if different from Report)

18. SUPPLEMENTARY NOTES

19. KEY WORDS (Continue on reverse side if necessary and identify by block number)

Axisymmetric Bodies
Turbulent Boundary Layer
Thick Stern Boundary Layer
Turbulence Length Scale
Turbulence Correlation Coefficient
Turbulence Reynolds Stress

20. ABSTRACT (Continue on reverse side if necessary and identify by block number)

Static pressure distributions, mean velocity profiles, distributions of turbulence intensities, and Reynolds stresses, spatial correlation coefficients, and the Taylor microscale of turbulence were measured across the stern boundary layer of an axisymmetric body with an inflected stern. A theoretical and numerical iteration scheme, which uses the boundary layer and open wake displacement body, is found to model satisfactorily

(Continued on reverse side)

DD FORM 1 JAN 73 1473 EDITION OF 1 NOV 65 IS OBSOLETE
S/N 0102-LF-014-6601

UNCLASSIFIED

SECURITY CLASSIFICATION OF THIS PAGE (When Data Entered)

17682

(Block 20 continued)

the viscid-inviscid interaction between the thick stern boundary layer and the external potential flow. The measured values of turbulence intensity, eddy viscosity, and mixing-length parameters in the stern region are found to be much smaller than those of a thin boundary layer. An approximate similarity characteristic for the thick axisymmetric stern boundary layer is obtained when the measured mixing-length parameters, the measured correlation length scales, and the measured Taylor microscales are normalized by the square root of the boundary-layer cross-sectional area instead of the local boundary layer thickness. When this simple similarity hypothesis for the mixing length and the displacement body is incorporated into the McDonnell Douglas Corp., Cebeci-Smith differential boundary-layer method, modified to consider the displacement body and wake, the theory predicts very well the measured distributions of the mean velocity throughout the entire stern boundary layer. The computation method developed earlier was found to predict well the boundary layer on convex sterns and is now found to apply equally well to the flow on inflected sterns.

TABLE OF CONTENTS

LIST OF FIGURES

LIST OF TABLES

NOTATION

A — Van Driest's damping factor, $A = 26\,\nu\left(\frac{\tau_w}{\rho}\right)^{-1/2}$

a_1 — Turbulence structure parameter, $a_1 = -\overline{u'v'}/q^2$

C_p — Pressure coefficient, $C_p = (p-p_0)\Big/\left(\frac{1}{2}\,\rho U_0^2\right) = 1 - (U_e/U_0)^2$

C_τ — Shear stress coefficient, $C_\tau = \frac{\tau_w}{p_t-p_s}\left(\frac{U_0}{U_e}\right)^2 = \frac{\tau_w^2}{\frac{1}{2}\,\rho\,U_e^2}$

D — Maximum diameter of the axisymmetric body

d_r — Radial separation distance between two points A and B, $d_r = r_B - r_A$

L — Total body length

L_E — Bow entrance length

ℓ — Mixing length parameter in the inner region,

$$\ell = 0.4\,r_0\,\ell n\left(\frac{r}{r_0}\right)\left\{1-\exp\left[-\frac{r_0}{A}\,\ell n\left(\frac{r}{r_0}\right)\right]\right\}$$

n — Tangent coordinate measured normal to the body meridian

n_c — Value of n at which $\varepsilon_i = \varepsilon_0$

n_δ — Value of boundary layer thickness normal to the body surface

p — Measured local static pressure

p_0 — Measured ambient pressure

p_s — Measured static pressure

p_t — Measured dynamic total pressure

q^2 — Turbulence parameter, $q^2 = \overline{u'^2} + \overline{v'^2} + \overline{w'^2}$

R_L	Reynolds number based on model length, $R_L = \frac{U_0 L}{\nu}$
R_λ	Axial turbulence Reynolds number, $R_\lambda = \frac{\sqrt{\overline{u_x'^2}}\,\lambda}{\nu}$
r	Radial coordinate measured from the axis of revolution normal to the x-axis
r_0	Body radius
r_{max}	Maximum body radius
s	Arclength coordinate measured parallel to the body meridian
U_e	Computed potential flow velocity on the displacement body
U_0	Free stream velocity
U_δ	Value of mean velocity component in the axial direction (u_x) at the radial position
u'	Turbulent velocity fluctuation in the axial direction
u_s	Mean velocity component in the s direction (parallel to the body meridian)
u_s'	Turbulent velocity fluctuation in the s direction
$\overline{u_s'v_n'}$	Reynolds stress
u_x	Mean velocity component in the axial direction
v'	Turbulent velocity fluctuation in the radial direction
v_n	Mean velocity component in the n direction (normal to the body meridian)
v_n'	Velocity fluctuation in the n direction
v_r	Mean velocity component in the radial direction

w' Turbulent velocity fluctuation in the azimuthal direction

x Axial coordinate measured from the nose of the body parallel to the axis of revolution

α $\tan^{-1}\left(\frac{dr_0}{dx}\right)$

γ_{tr} $\cong \left[1+5.5\left(\frac{n}{\delta}\right)\right]^{-1}$, intermittency factor

δ Boundary layer thickness where $u_s/U_e = 0.995$, $\delta = \delta_{0.995}$

δ_r Radial boundary layer thickness

δ_p^* Planar displacement thickness, $\delta_p^* = \int_0^{\delta_r}\left(1-\frac{u_x}{U_\delta}\right)dr$

δ_r^* Axisymmetric displacement thickness

ε Eddy viscosity

ε_i Eddy viscosity in the inner region, $\varepsilon_i = \ell^2\left(\frac{r}{r_0}\right)\frac{\partial u_s}{\partial n}$

ε_0 Eddy viscosity in the outer region, $\varepsilon_0 = 0.0168\, U_e\, \delta_p^*\, \gamma_{tr}$

η Nondimensional correlation distance

θ_p Planar momentum thickness, $\theta_p = \int_0^{\delta_r}\left(1-\frac{u_x}{U_\delta}\right)\frac{u_x}{U_\delta}\,dr$

Λ Axisymmetric displacement area, $\Lambda = \int_{r_0}^{\delta_r}\left(1-\frac{u_x}{U_\delta}\right)r\,dr$

λ Microscale of the turbulence, $\lambda^2 = \dfrac{\overline{u_x'^2}\ \overline{u_x^2}}{\overline{\left(\dfrac{\partial u_x'}{\partial t}\right)^2}}$

ν Kinematic viscosity of the fluid

ρ Mass density of the fluid

$\rho_{AB}(d_r)$ Spatial correlation coefficient of two axial velocity fluctuations at points A and B, $\rho_{AB}(d_r) = \overline{u_A' u_B'} \Big/ \sqrt{\overline{u_A'^2}}\sqrt{\overline{u_B'^2}}$

τ_w Shear stress at the wall

Ω Axisymmetric momentum area, $\Omega = \displaystyle\int_{r_0}^{\delta_r} \left(1 - \frac{u_x}{U_\delta}\right)\frac{u_x}{U_\delta}\, r\, dr$

ABSTRACT

Static pressure distributions, mean velocity profiles, distributions of turbulence intensities, and Reynolds stresses, spatial correlation coefficients, and the Taylor microscale of turbulence were measured across the stern boundary layer of an axisymmetric body with an inflected stern. A theoretical and numerical iteration scheme, which uses the boundary layer and open wake displacement body, is found to model satisfactorily the viscid-inviscid interaction between the thick stern boundary layer and the external potential flow. The measured values of turbulence intensity, eddy viscosity, and mixing-length parameters in the stern region are found to be much smaller than those of a thin boundary layer. An approximate similarity characteristic for the thick axisymmetric stern boundary layer is obtained when the measured mixing-length parameters, the measured correlation length scales, and the measured Taylor microscales are normalized by the square root of the boundary-layer cross-sectional area instead of the local boundary layer thickness. When this simple similarity hypothesis for the mixing length and the displacement body is incorporated into the McDonnell Douglas Corp., Cebeci-Smith differential boundary-layer method, modified to consider the displacement body and wake, the theory predicts very well the measured distributions of the mean velocity throughout the entire stern boundary layer. The computation method developed earlier was found to predict well the boundary layer on convex sterns and is now found to apply equally well to the flow on inflected sterns.

ADMINISTRATIVE INFORMATION

The work described in this report was funded under the David W. Taylor Naval Ship Research and Development Center's Independent Research Program, Program Element 61152N, Project Number ZR 000 01, and Work Unit 1552-103.

INTRODUCTION

This report presents measurements of the turbulent boundary layer characteristics in the thick stern boundary layer of an axisymmetric body with an extremely full inflected stern. These measurements include the distributions of pressure coefficient and shear stress on the body, static pressure distribution across the stern boundary layer, mean velocity profiles, turbulence intensities, Reynolds stresses, eddy viscosity, mixing

length, and spatial correction function. This investigation is an extension of the earlier research on convex axisymmetric thick stern boundary layers reported by Huang, et al.[1,2*]

The experimental measurements are compared with the results computed by the method of Wang and Huang[3] for computing the potential flow-boundary layer interaction on axisymmetric bodies. The initial step in this procedure begins with the computation of the potential-flow pressure distribution on the body using the computer code of Hess and Smith.[4] The McDonnell Douglas Corp., Cebeci-Smith** method[5] is then used to calculate the flow over the body and the integral relations of Granville[6] are used to calculate the flow in the wake. The local displacement thickness computed in these boundary layer calculations is added to the original body to obtain a modified body and wake geometry as suggested by Preston[7] and Lighthill.[8] The procedure is repeated until the pressure distributions on the body from two successive approximations agree to within a given error criterion. This iterative scheme is referred to as the displacement body concept.

Several modifications have been made to the Douglas C-S differential boundary layer method[5] by Wang and Huang.[3] These changes were incorporated to improve the comparison of the thick boundary layer parameters with the experimental data of Huang et al.[1] and Patel and Lee.[9] Transverse curvature effects are included in the solution of the standard thin boundary layer equations in the Wang and Huang method. Effects due to longitudinal curvature are neglected. The pressure variation across the boundary layer is obtained from potential flow calculations for the final displacement body. The mixing length and eddy viscosity in the thick boundary layer region are obtained by modifying the thin boundary layer values by factors which are proportional to the annular area between the body surface and the edge of the boundary layer.

In the stern and near-wake region ($0.95 \leq x/L \leq 1.05$), where x is the axial distance from the nose and L is the total body length, a fifth degree

---

*A complete listing of references is given on page 51.

**The McDonnell Douglas Corp., Cebeci-Smith method will hereafter be designated as Douglas C-S.

polynomial was used to determine the boundary layer flow. The coefficients for this polynomial were determined by the conditions that the thickness, slope, and curvature be equal to those calculated by the modified boundary-layer method at x/L = 0.95 and by the Granville integral wake relations[6] at x/L = 1.05. This method was found by Huang et al.[1] to give excellent agreement with experimental values of pressure, shear stress, and velocity profiles over the forward 90 percent of the bodies investigated. As the boundary-layer thicknesses became larger, particularly when these thicknesses became greater than the radii of the bodies, the measured values of shear stress and velocity became smaller than those predicted by the theory.

In the following discussion, the experimental techniques and geometries of the model are given in detail. The experimental and theoretical results are compared and the measured turbulence characteristics are presented. The method of obtaining the eddy viscosity and mixing length is discussed and the experimentally-determined distributions are given. The concept of similarity length-scale in the thick stern boundary layer is examined experimentally. The square root of the annular area between the body surface and the edge of the boundary layer is found to be the appropriate length scale for the axisymmetric thick stern boundary layer.

WIND TUNNEL AND MODEL

The experimental investigation was conducted in the DTNSRDC anechoic wind tunnel facility. The wind tunnel has a closed jet test section that is 8 ft (2.4 m) square and 13.75 ft (4.19 m) long. The corners have fillets which are carried through the contraction. The test section is followed by an acoustically-lined large chamber 23.5 ft (7.16 m) long. It was found previously by Huang et al.,[1] that the ambient free-stream turbulence levels, $(\sqrt{\overline{u'^2}}/U_0) \times 100$, are 0.075, 0.090, 0.100, and from 0.12 to 0.15 for free-stream velocities U_0 of 24.4, 30.5, 38.1, and 45.7 m/s, respectively. Integration of the measured noise spectrum levels in the test section from 10 to 10,000 Hz indicated that the typical background

acoustic noise levels at 30.5 m/s were about 93 dB re 0.0002 dyn/cm^2 (0.0002 Pa). These levels of ambient turbulence and acoustic noise were considered low enough so as not to unfavorably affect the measurements of boundary-layer characteristics. The maximum air speed which can be achieved is 200 ft/sec (61 m/s); in the present experiments the wind tunnel velocity was held constant at 150 ft/sec (45.72 m/s).

An axisymmetric inflected (convex and concave) afterbody with a bow-entrance length-to-diameter ratio (L_E/D) of 2.05 was used for the present experimental investigation. The detailed offsets are given in Table 1. Figure 1 shows a comparison of the present afterbody (Afterbody 5) and Afterbodies 1 and 2 previously investigated by Huang et al.[1,2] The contour of Afterbody 5 changes from convex to concave at x/L = 0.913, whereas Afterbodies 1 and 2 are convex up to x/L = 0.96. Afterbody 5 is connected to a parallel middle body which is 6.0 ft (1.83 m) long and an existing streamlined forebody with a bow-entrance length-to-diameter ratio (L_E/D) of 1.82. The total model length is 9.55 ft (2.91 m) with a maximum forebody diameter of 0.917 ft (0.28 m).

The model was supported by two streamlined struts separated by one-third of the model length. The upstream strut had a 15-cm chord and the downstream strut a 3-cm chord. The disturbances generated by the supporting struts were within the region below the horizontal centerplane, therefore, all of the experimental data were taken above the model on the vertical centerplane along the upper meridian where there was little effect from the supporting struts. One-half of the model length protruded beyond the closed-jet working section into the open-jet section. The ambient static pressure coefficients across and along the entire open-jet chamber (7.2 m × 7.2 m × 6.4 m) were found to vary less than 0.3 percent of the dynamic pressure. Tunnel blockage and longitudinal pressure gradient effects along the tunnel length were almost completely removed by testing the afterbody in the open-jet section.

The location of the boundary-layer transition from laminar to turbulent flow was artificially induced by a 0.024 in. (0.61 mm) diameter trip wire located at x/L = 0.05. Huang et al.[1] found that the trip wire

TABLE 1 - MODEL OFFSETS

x/L	r_0/L	r_0/r_{max}	x/L	r_0/L	r_0/r_{max}	x/L	r_0/L	r_0/r_{max}
0.0000	0.0000	0.0000	.4450	.0480	1.0000	.7768	.0480	1.0000
.0052	.0105	.2193	.4659	.0480	1.0000	.7821	.0480	1.0000
.0105	.0150	.3118	.4868	.0480	1.0000	.7863	.0480	1.0000
.0157	.0184	.3835	.5078	.0480	1.0000	.7905	.0480	1.0000
.0209	.0213	.4441	.5256	.0480	1.0000	.7936	.0480	1.0000
.0262	.0239	.4975	.5402	.0480	1.0000	.7967	.0480	1.0000
.0314	.0262	.5454	.5518	.0480	1.0000	.8000	.0480	1.0000
.0366	.0283	.5891	.5601	.0480	1.0000	.8030	.0480	1.0000
.0419	.0302	.6291	.5675	.0480	1.0000	.8062	.0480	.9998
.0471	.0320	.6659	.5727	.0480	1.0000	.8093	.0479	.9991
.0523	.0336	.7000	.5779	.0480	1.0000	.8135	.0479	.9975
.0576	.0351	.7315	.5832	.0480	1.0000	.8187	.0477	.9937
.0628	.0365	.7607	.5884	.0480	1.0000	.8256	.0473	.9852
.0681	.0378	.7877	.5936	.0480	1.0000	.8308	.0468	.9756
.0733	.0390	.8126	.5989	.0480	1.0000	.8360	.0462	.9632
.0785	.0401	.8356	.6041	.0480	1.0000	.8413	.0455	.9478
.0838	.0411	.8567	.6093	.0480	1.0000	.8465	.0446	.9296
.0890	.0420	.8760	.6146	.0480	1.0000	.8517	.0436	.9085
.0942	.0429	.8936	.6198	.0480	1.0000	.8570	.0425	.8847
.0995	.0437	.9097	.6250	.0480	1.0000	.8622	.0412	.8583
.1047	.0443	.9241	.6303	.0480	1.0000	.8674	.0398	.8294
.1099	.0450	.9371	.6355	.0480	1.0000	.8727	.0383	.7983
.1152	.0455	.9486	.6407	.0480	1.0000	.8779	.0367	.7652
.1204	.0460	.9587	.6460	.0480	1.0000	.8831	.0350	.7303
.1256	.0464	.9676	.6512	.0480	1.0000	.8884	.0333	.6939
.1309	.0468	.9751	.6564	.0480	1.0000	.8936	.0315	.6561
.1361	.0471	.9816	.6617	.0480	1.0000	.8988	.0296	.6174
.1413	.0474	.9869	.6669	.0480	1.0000	.9041	.0277	.5778
.1466	.0476	.9911	.6722	.0480	1.0000	.9093	.0258	.5378
.1518	.0477	.9945	.6774	.0480	1.0000	.9145	.0239	.4975
.1570	.0478	.9969	.6826	.0480	1.0000	.9198	.0219	.4574
.1623	.0479	.9986	.6879	.0480	1.0000	.9250	.0200	.4176
.1675	.0480	.9996	.6931	.0480	1.0000	.9303	.0182	.3784
.1727	.0480	1.0000	.6983	.0480	1.0000	.9355	.0163	.3402
.1801	.0480	1.0000	.7036	.0480	1.0000	.9407	.0145	.3032
.1895	.0480	1.0000	.7088	.0480	1.0000	.9460	.0129	.2678
.2010	.0480	1.0000	.7140	.0480	1.0000	.9512	.0113	.2345
.2146	.0480	1.0000	.7193	.0480	1.0000	.9564	.0098	.2035
.2303	.0480	1.0000	.7245	.0480	1.0000	.9617	.0084	.1757
.2481	.0480	1.0000	.7297	.0480	1.0000	.9669	.0073	.1517
.2670	.0480	1.0000	.7350	.0480	1.0000	.9721	.0064	.1326
.2879	.0480	1.0000	.7402	.0480	1.0000	.9774	.0058	.1199
.3089	.0480	1.0000	.7454	.0480	1.0000	.9826	.0055	.1149
.3298	.0480	1.0000	.7507	.0480	1.0000	.9832	.0055	.1148
.3507	.0480	1.0000	.7559	.0480	1.0000	.9874	.0053	.1108
.3717	.0480	1.0000	.7611	.0480	1.0000	.9916	.0048	.0994
.3926	.0480	1.0000	.7664	.0480	1.0000	.9958	.0036	.0744
.4136	.0480	1.0000	.7716	.0480	1.0000	1.0000	0.0000	0.0000
.4240	.0480	1.0000						

MODEL 5225-5

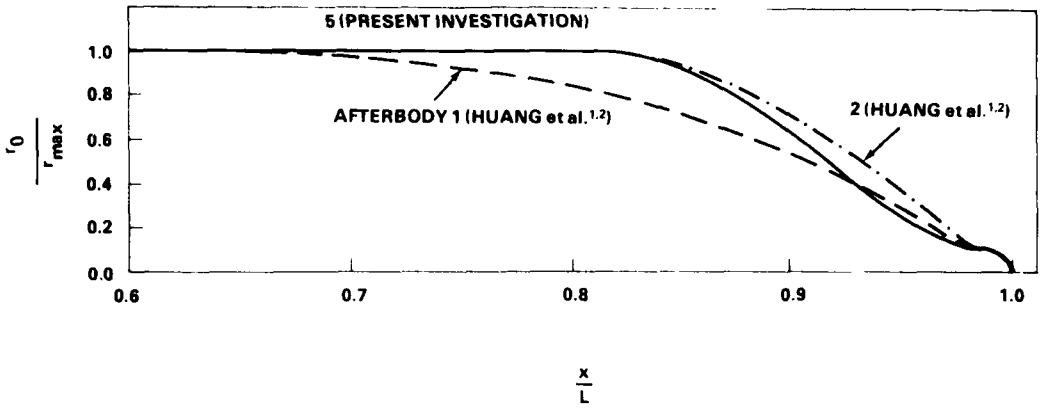

Figure 1 - Three Afterbodies

effectively tripped the flow 0.39 in. (1 cm) downstream from the wire and, because of the finite parasitic drag of the wire, the boundary-layer can be considered to become turbulent at a virtual origin 5.4 in. (13.7 cm) upstream from the trip wire at a Reynolds number of 9.3×10^6. The virtual origin for the turbulent flow is defined such that the sum of the laminar frictional drag from the nose to the trip wire, the parasitic drag of the trip wire, and the turbulent frictional drag aft of the trip wire is equal to the sum of the laminar frictional drag from the nose to the virtual origin and the turbulent frictional drag from the virtual origin to the after end of the model (similar to Reference 10). The virtual origin location was taken as the transition location at which the boundary-layer changed from laminar to turbulent in the boundary-layer calculations.

INSTRUMENTATION

A Preston tube with a 0.072 in. (1.83 mm) inside diameter was attached and alined with the flow on the upper meridian of the stern to measure the shear stress distribution. The Preston tube was calibrated in a 1 in. (2.54 cm) diameter water-pipe flow facility described by Huang and von Kerczek.[11] A series of 0.031 in. (0.8 mm) diameter pressure taps were embedded on the upper meridian of the stern at the Preston tube locations. These pressure taps were connected to a multiple pressure scanivalve system

that takes one integral pressure transducer with its zeroing circuit and measures a single pressure in sequence along the stern upper meridian. The pressure transducer used was designed for measuring low pressure up to 0.2 psi (1.379×10^3 Pa). The zero-drift linearity, scanivalve, hysteresis, and pressure transducer with zeroing circuit were carefully checked and the overall accuracy was found to be within 0.5 percent of the dynamic pressure.

A Prandtl-type static pressure probe of 0.123 in. (3.125 mm) diameter with four equally spaced holes located three probe diameters after the probe nose was used to measure the static pressure across the boundary layer. By yawing the probe in the free stream, it was found that the measured static pressure was insensitive to the probe angle up to a 5-degree yaw. In all cases, the static pressure probe remained in alinement by less than 5-degree yaw.

The mean axial and radial velocities and the turbulence intensities for the Reynolds stress calculations were measured by a TSI, Inc. Model 1241-20 "X" type hot-film probe. The probe elements are 0.002 in. (0.05 mm) in diameter with a sensing length of 0.04 in. (1.0 mm). The spacing between the two cross elements is 0.04 in. (1.0 mm). A typical schematic of the hot-film probe used is shown in Figure 2. A two-channel hot-wire and hot-film anemometer with linearizers was used to monitor the response of the hot-film probe. A temperature compensating sensor (probe) was used with each hot-film element to regulate the operating temperature of the sensor with the changes in air temperature. The "X" hot film and its temperature-compensated sensor were calibrated together through the expected air temperature range and supplied with their individual linearization polynomial coefficients at the factory. A single element TSI, Inc. Model 1212-TI.5 hot-wire probe also was used to measure the velocity distribution across the stern boundary layer. Two single-element TSI (Model 1212) hot-wire probes with a 90-deg bend separated by a small radial distance also were used to measure spatial correlation functions in the thick boundary layer.

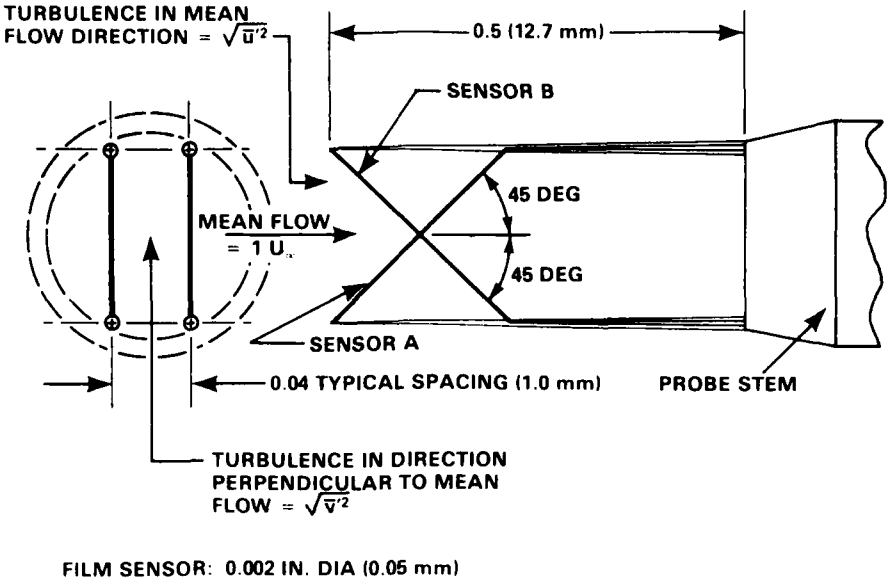

Figure 2 - Schematic of a Two Element Sensor Alined 90 Degrees to Each Other and 45 Degrees to Probe Axis

The frequency response of the anemometer system, for reliable measurements claimed by the manufacturer, is 0 to 200 kHz. Calibration of the "X" hot film was made before and after each set of measurements. It was found that the hot-film anemometer system had a $\pm$0.5 percent accuracy, $\pm$0.75 ft/sec ($\pm$0.23 m/s) accuracy at the free stream velocity of 150 ft/sec (45.72 m/s), during the entire experiment. An estimate was made of the cross-flow velocity by yawing the "X" hot-film probe in the freestream. It was found that the crossflow velocities were about one percent of the freestream velocity.

The linearized signals were fed into a Time/Data Model 1923-C real-time analyzer. Both channels of the analog signal were digitized at a rate of 128 points per second for 8 seconds. These data were immediately analyzed by a computer to obtain the individual components of mean velocity, turbulence fluctuation, and Reynolds stress on a real time basis.

A traversing system with a streamlined strut was mounted on a guide plate that permitted the traverse to be locked in various stationary positions parallel to the longitudinal model axis.

COMPARISON OF EXPERIMENTAL AND THEORETICAL RESULTS

Two coordinate systems for an axisymmetric body are given in Figure 3. The coordinate system used to experimentally measure the boundary-layer

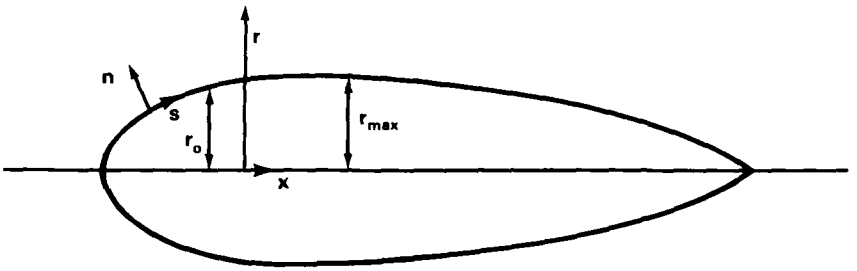

Figure 3 - Axisymmetric Coordinate Systems

flow and to report the results is the x-r coordinate system. The axial coordinate x is measured from the nose of the body parallel to the axis of revolution. The radial component r is measured from the axis of revolution and is normal to the x-axis. The curvilinear s-n coordinate system is used in the Douglas C-S differential boundary layer method.[5] The arclength coordinate s is measured parallel to the body meridian and the tangent coordinate n is measured normal to the body meridian.

The Douglas C-S boundary layer method is used in conjunction with the displacement body concept to predict the flow over the body. Wang and Huang[3] have made several modifications to the Douglas C-S code in an attempt to better model a thick stern boundary layer. A comparison of their original theory with experimental results is given by Huang et al.[1] That comparison revealed several inadequacies in the theory. Wang and Huang[3] subsequently modified their original method based on these experimental comparisons. The new modifications are evaluated in the present investigation. The mixing length in the thick stern boundary layer region is modeled by a simple algebraic formula proposed by Huang et al.[1] This formulation includes only transverse curvature effects. The eddy viscosity

in the outer region was also modified by an algebraic formula with the intention of improving the accuracy of the velocity profiles near the body in the thick boundary layer region. The final modification to the original method uses the predicted potential flow velocities outside of the displacement body to modify the velocities in the direction parallel to the body meridian tangent.

MEASURED AND COMPUTED PRESSURE AND SHEAR STRESS DISTRIBUTIONS

Pressure taps were used to measure the steady pressure at 15 selected locations along the stern surface of the axisymmetric body. The pressure coefficient, C_p, is computed from the measured pressures by the relationship

$$C_p = \frac{p-p_0}{p_t-p_s} = \frac{p-p_0}{\frac{1}{2}\rho U_0^2} \tag{1}$$

where p = measured local static pressure

p_0 = measured ambient pressure

p_t = measured dynamic total pressure

p_s = measured static pressure

ρ = mass density of the fluid

The analytically-predicted pressure coefficient was computed on the displacement body using the Douglas-Neumann potential flow method of Hess and Smith[4] and is given by

$$C_p = 1 - \left(\frac{U_e}{U_0}\right)^2 \tag{2}$$

where U_e is the computed potential flow velocity on the displacement body and U_0 is the freestream velocity, 150 ft/sec (45.72 m/s).

A comparison of the measured and theoretical values of the pressure coefficient on the surface of the axisymmetric body under consideration is given in Figure 4. The theory underpredicts the magnitude of the minimum C_p value slightly; the theoretical trough is not as full as the measured

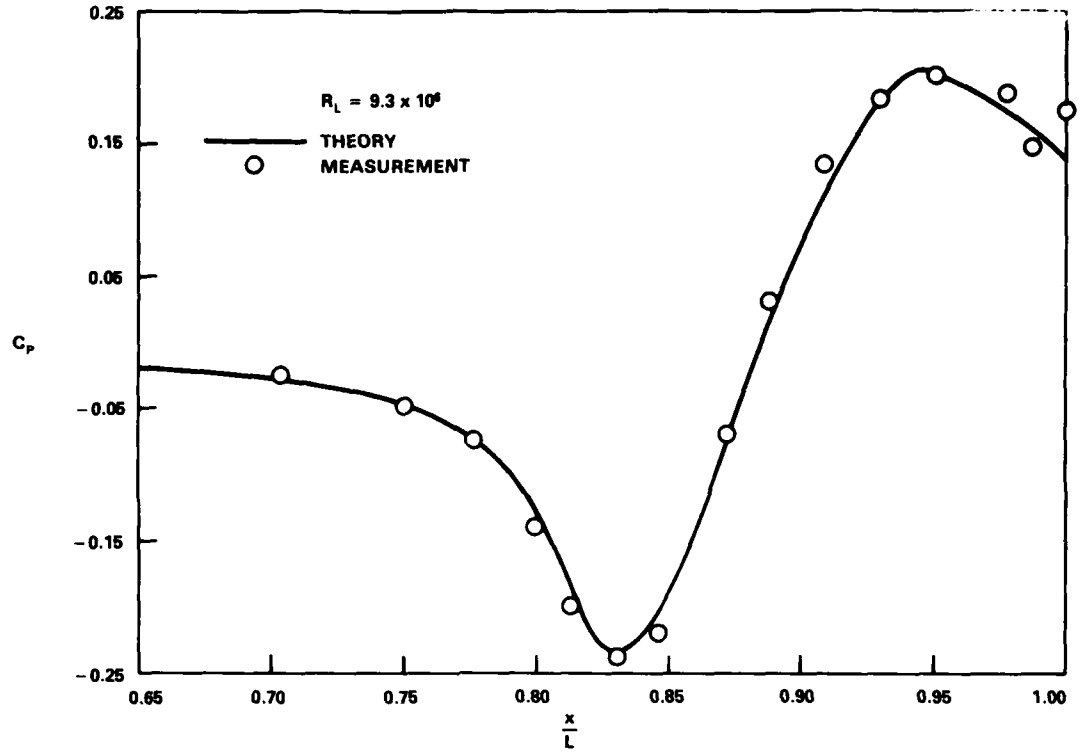

Figure 4 - Computed and Measured Stern Pressure Distribution on Afterbody 5

trough. The three measured values of C_p for $\frac{x}{L} \geq 0.975$ fluctuate somewhat about the theoretical curve for C_p. These discrepancies are small, and overall agreement between theoretical and measured values of the pressure coefficient is considered excellent.

Readings from a Preston tube, which was taped to the stern surface at the pressure tap locations, were used in conjunction with the steady pressure readings to obtain the shear stress distribution at the body surface. The calibration curve, presented by Huang and von Kerczek,[11] for a

Preston tube in a pipe was used to compute the shear stress at the wall, τ_w. The shear stress coefficient C_τ is given by

$$C_\tau = \frac{\tau_w}{p_t - p_s}\left(\frac{U_0}{U_e}\right)^2 \tag{3}$$

for the measured shear stress and by

$$C_\tau = \frac{\tau_w}{\frac{1}{2}\rho U_e^2} \tag{4}$$

for the analytical shear stress.

Figure 5 shows a comparison of the measured and theoretical values of the shear stress coefficient. Agreement is good for values of $\frac{x}{L} < 0.9$. The trough, which occurs for $\frac{x}{L} > 0.9$, is somewhat overpredicted by the theory. This discrepancy in the distribution of the shear stress coefficients indicates that the present analytical model may be inadequate for the precise prediction of the shear stress on the last ten percent of the body. The measured values of C_p and C_τ are tabulated in Table 2.

MEASURED AND COMPUTED STATIC PRESSURE DISTRIBUTION

The measured and computed static pressure coefficients for Afterbody 5 are compared in Figure 6 at various locations across the stern boundary layer. The off-body option of the Douglas potential-flow computer code was used to compute the static pressure distributions for the displacement body (solid lines) and the actual body (broken lines). As can be seen in Figure 6, except at x/L = 0.704, 0.987, and 1.045, the measured static pressure distributions agree better with the theoretical pressure distributions computed from the displacement-body model than those from the original body. At x/L = 0.704, 0.987, and 1.045, the two calculation methods agree to within one percent. The discrepancy between the measured

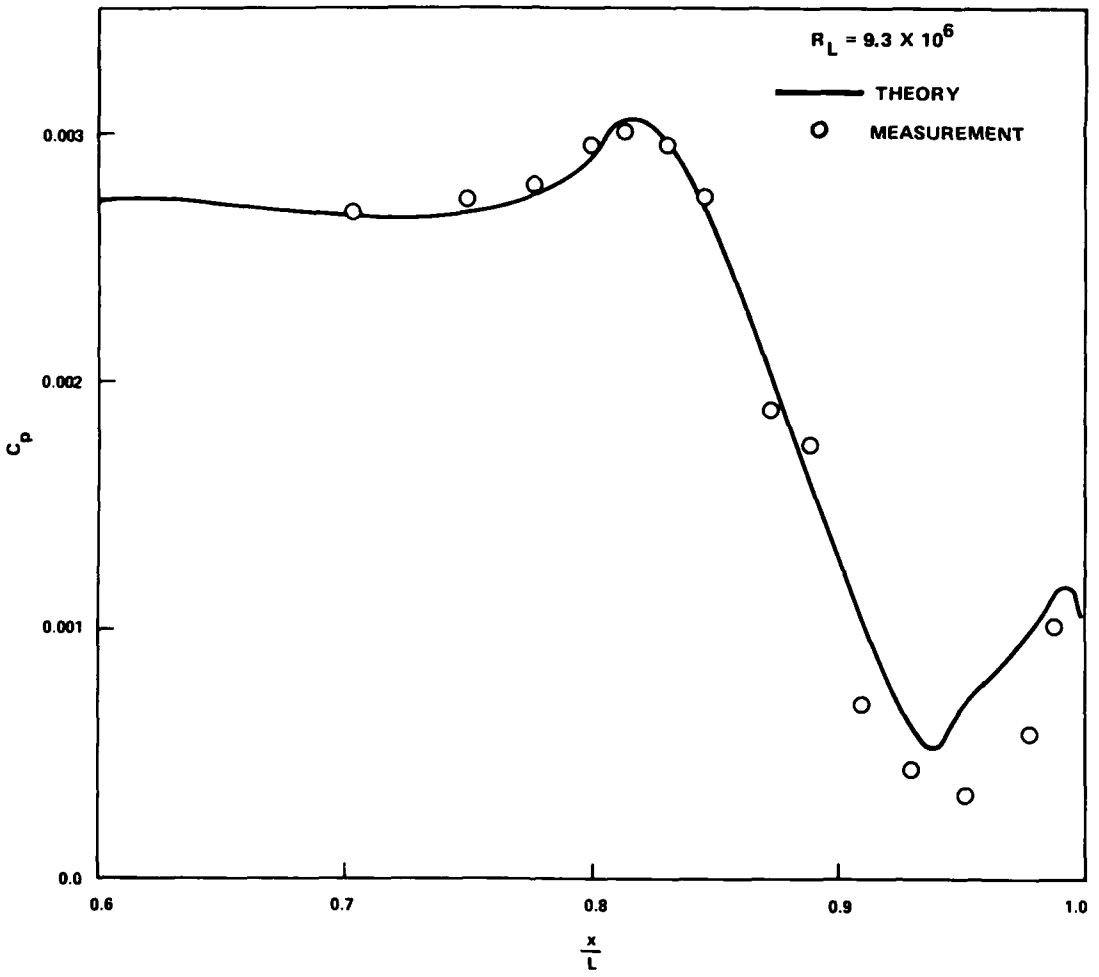

Figure 5 - Computed and Measured Shear Stress Distribution on Afterbody 5

TABLE 2 - MEASURED PRESSURE AND SHEAR STRESS COEFFICIENTS

x/L	r_0/r_{max}	C_p	C_τ
0.7036	1.0000	-0.024	0.00268
0.7507	1.0000	-0.048	0.00272
0.7768	1.0000	-0.075	0.00278
0.8000	1.0000	-0.140	0.00294
0.8135	0.9975	-0.200	0.00300
0.8308	0.9756	-0.238	0.00295
0.8465	0.9296	-0.220	0.00274
0.8727	0.7983	-0.070	0.00188
0.8884	0.6939	+0.030	0.00174
0.9093	0.5378	+0.133	0.00069
0.9303	0.3784	+0.182	0.00043
0.9512	0.2345	+0.201	0.00034
0.9774	0.1199	+0.186	0.00058
0.9874	0.1108	+0.146	0.00101
1.0000	0.0000	+0.173	---

Figure 6 - Computed and Measured Static Pressure Distributions Across Stern Boundary Layer of Afterbody 5

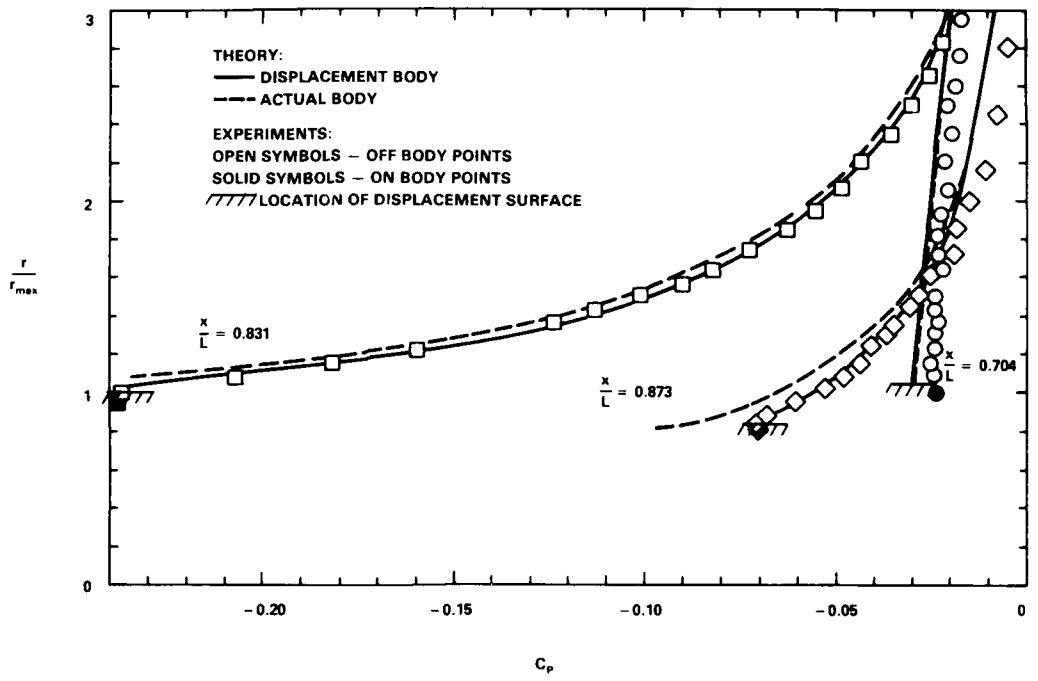

Figure 6a - Nondimensional Axial Lengths, x/L = 0.704, 0.831, 0.873

Figure 6 (Continued)

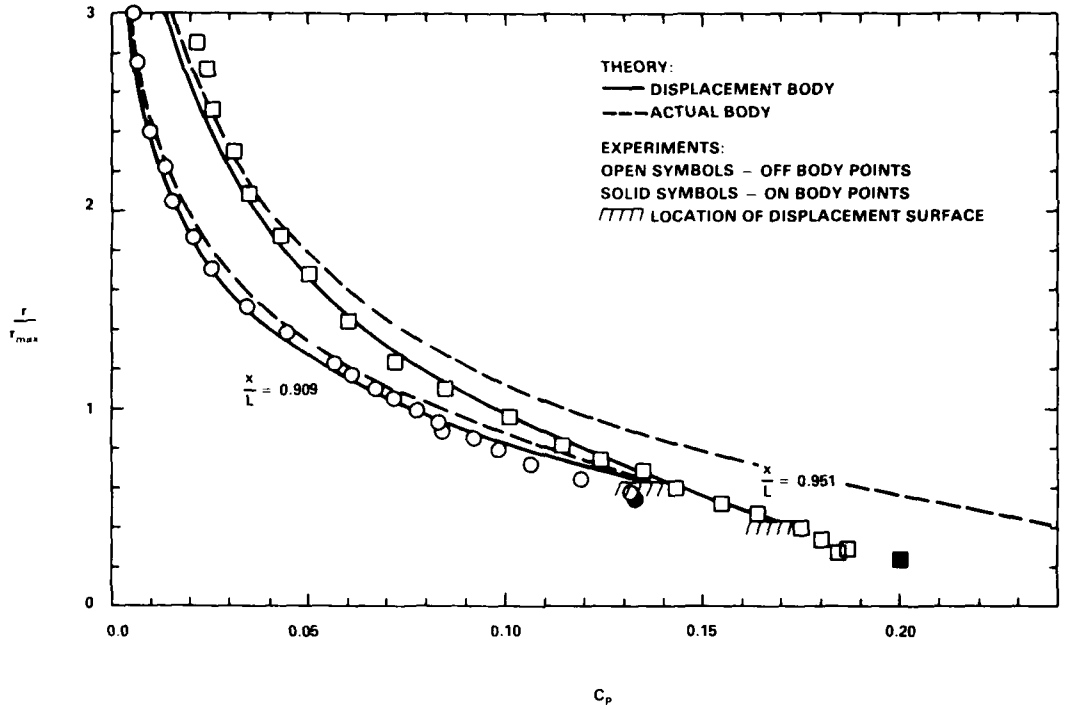

Figure 6b - Nondimensional Axial Lengths, x/L = 0.951, 0.909

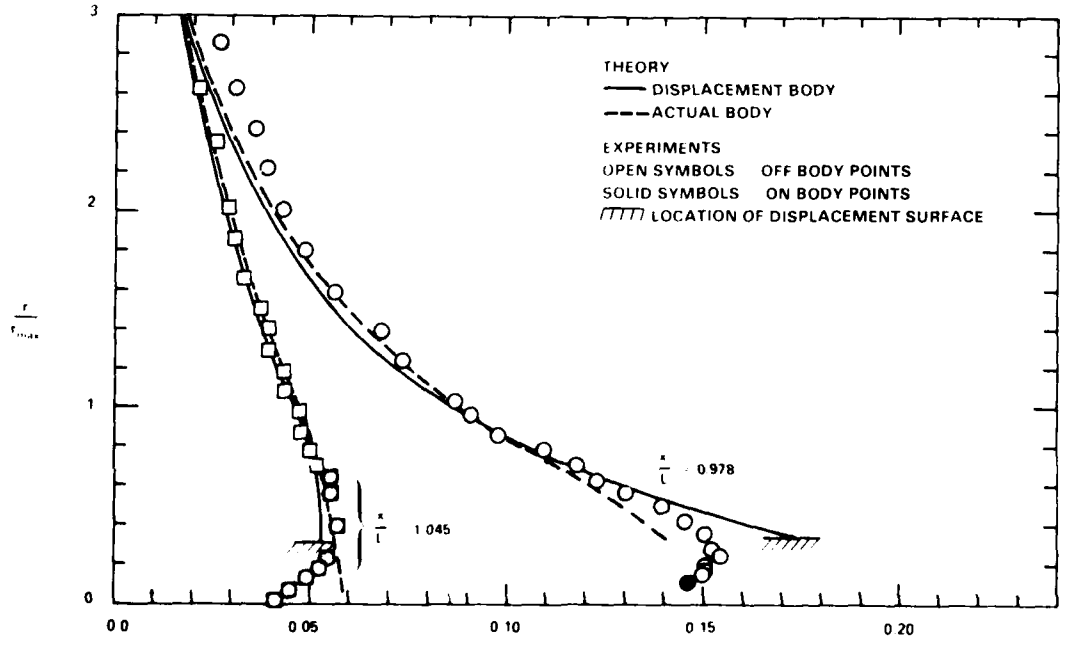

Figure 6c - Nondimensional Axial Lengths, x/L = 0.987, 1.045

and computed (by displacement-body model) values of C_p is, in general, less than 0.01 which is about the accuracy of the measurement. The measured values of C_p are tabulated in Table 3.

As will be seen later, the displacement body of Afterbody 5 is convex from the parallel middle body up to x/L = 0.898 and becomes concave downstream from x/L > 0.90, which is rather close to the inflection point of the actual body (x/L = 0.913). The differences in the theoretical values of off-body pressure distributions computed from the displacement body and the actual body are very noticeable at x/L = 0.951 where the measured pressure distributions agree rather well with the distributions computed from the displacement-body model. The close agreement between the computed displacement-body and measured static pressure distributions for Afterbody 5, as well as Afterbodies 1 and 2 (Reference 1), support the displacement-body concept for computing the potential flow outside of the displacement surface. The pressure coefficients inside the displacement body may be more accurately calculated by a streamline curvature method proposed by Dyne.[12] However, in the present calculation method the value of C_p is assumed to be constant inside the displacement body. The maximum error of the value of C_p from this approximation is less than 2 percent inside the displacement body (Figure 6).

MEASURED AND COMPUTED MEAN VELOCITY PROFILE

MEASUREMENT

The axial and radial mean velocity components were measured by the "X" hot-film sensor. At a given axial location, measurements were taken at numerous radial positions to obtain the velocity profile. The hot-film probe was mounted with the sensing elements in a vertical position. At each radial position, 1024 data values were collected in 8 seconds. The linearized data were input to a computer code which calculated and printed the values of the mean velocity components u_x in the axial direction and v_r in the radial direction (given in Table 4).

A single element hot-wire sensor also was used to compare with the results of the "X" sensor. The values of the axial mean velocity component

TABLE 3 - MEASURED STATIC PRESSURE COEFFICIENTS ACROSS STERN BOUNDARY LAYER AND NEAR WAKE

x/L = 0.7036			x/L = 0.8308		
r/r_{max}	$(r-r_0)/r_{max}$	C_p	r/r_{max}	$(r-r_0)/r_{max}$	C_p
1.0000	0.0000	-0.0240	0.9756	0.0000	-0.2380
1.0873	0.0873	-0.0242	0.9938	0.0182	-0.2372
1.1576	0.1576	-0.0251	1.0711	0.0955	-0.2072
1.2349	0.2349	-0.0222	1.1484	0.1728	-0.1821
1.2981	0.2981	-0.0242	1.2187	0.2431	-0.1599
1.3614	0.3614	-0.0232	1.2890	0.3134	-0.1412
1.4317	0.4317	-0.0242	1.3663	0.3907	-0.1240
1.5090	0.5090	-0.0241	1.4366	0.4610	-0.1132
1.5792	0.5792	-0.0241	1.4998	0.5242	-0.1019
1.6495	0.6495	-0.0227	1.5631	0.5875	-0.0901
1.7198	0.7198	-0.0232	1.6404	0.6648	-0.0827
1.8252	0.8252	-0.0232	1.7458	0.7702	-0.0723
1.9377	0.9377	-0.0227	1.8442	0.8686	-0.0625
2.0642	1.0642	-0.0207	1.9567	0.9810	-0.0551
2.2118	1.2118	-0.0217	2.0621	1.0865	-0.0482
2.3523	1.3523	-0.0197	2.2027	1.2270	-0.0433
2.4929	1.4929	-0.0207	2.3432	1.3676	-0.0354
2.6335	1.6335	-0.0182	2.4978	1.5222	-0.0300
2.7740	1.7740	-0.0172	2.6595	1.6839	-0.0251
2.9497	1.9497	-0.0168	2.8352	1.8596	-0.0222
3.1254	2.1254	-0.0138	3.1233	2.1477	-0.0128
3.3082	2.3082	-0.0153	3.3834	2.4078	-0.0103
3.4768	2.4768	-0.0133	3.6083	2.6327	-0.0049
3.7228	2.7228	-0.0123			

TABLE 3 (Continued)

x/L = 0.8727			x/L = 0.9093		
r/r_{max}	$(r-r_0)/r_{max}$	C_p	r/r_{max}	$(r-r_0)/r_{max}$	C_p
0.7983	0.0000	-0.0700	0.5378	0.0000	+0.1330
0.8220	0.0236	-0.0709	0.5687	0.0309	+0.1318
0.8853	0.0869	-0.0680	0.6390	0.1012	+0.1190
0.9555	0.1572	-0.0611	0.7093	0.1715	+0.1067
1.0188	0.2204	-0.0527	0.7866	0.2488	+0.0984
1.0961	0.2977	-0.0480	0.8428	0.3050	+0.0920
1.1594	0.3610	-0.0434	0.8780	0.3402	+0.0984
1.2296	0.4313	-0.0409	0.9272	0.3893	+0.0831
1.2999	0.5016	-0.0365	0.9834	0.4456	+0.0772
1.3772	0.5789	-0.0350	1.0466	0.5088	+0.0718
1.4475	0.6491	-0.0301	1.0958	0.5580	+0.0669
1.5178	0.7194	-0.0287	1.1731	0.6353	+0.0610
1.6162	0.8178	-0.0252	1.2294	0.6916	+0.0566
1.7216	0.9232	-0.0192	1.3840	0.8462	+0.0442
1.8622	1.0638	-0.0183	1.5175	0.9797	+0.0344
2.0027	1.2044	-0.0148	1.7003	1.1624	+0.0255
2.1433	1.3449	-0.0104	1.8619	1.3241	+0.0206
2.4525	1.6542	-0.0074	2.0446	1.5068	+0.0152
2.8110	2.0126	-0.0044	2.2203	1.6825	+0.0132
3.1624	2.3640	+0.0010	2.3960	1.8582	+0.0097
3.4505	2.6522	+0.0049	2.7475	2.2096	+0.0072
			2.9583	2.4205	+0.0062
			3.2043	2.6665	+0.0067

TABLE 3 (Continued)

x/L = 0.9512			x/L = 0.9874		
r/r_{max}	$(r-r_0)/r_{max}$	C_p	r/r_{max}	$(r-r_0)/r_{max}$	C_p
0.2345	0.0000	+0.2010	0.1108	0.0000	+0.1460
0.2655	0.0309	+0.1845	0.1245	0.0136	+0.1488
0.2795	0.0450	+0.1869	0.1527	0.0418	+0.1497
0.3287	0.0942	+0.1802	0.1737	0.0628	+0.1507
0.3920	0.1574	+0.1751	0.2300	0.1191	+0.1536
0.4693	0.2347	+0.1642	0.2721	0.1612	+0.1517
0.5325	0.2980	+0.1549	0.3494	0.2385	+0.1497
0.6028	0.3683	+0.1430	0.4197	0.3088	+0.1448
0.6801	0.4456	+0.1351	0.4900	0.3791	+0.1388
0.7434	0.5088	+0.1243	0.5603	0.4494	+0.1304
0.8136	0.5791	+0.1144	0.6306	0.5197	+0.1225
0.9542	0.7197	+0.1011	0.7009	0.5899	+0.1171
1.0948	0.8602	+0.0848	0.7711	0.6602	+0.1092
1.2353	1.0008	+0.0719	0.8414	0.7305	+0.0978
1.4462	1.2116	+0.0601	0.9539	0.8430	+0.0904
1.6641	1.4295	+0.0503	1.0241	0.9132	+0.0865
1.8679	1.6333	+0.0429	1.2350	1.1241	+0.0727
2.0857	1.8512	+0.0350	1.3685	1.2576	+0.0678
2.2966	2.0620	+0.0310	1.5864	1.4755	+0.0555
2.5004	2.2659	+0.0256	1.7902	1.6793	+0.0481
2.7112	2.4767	+0.0241	2.0011	1.8902	+0.0422
2.9291	2.6946	+0.0212	2.2119	2.1010	+0.0387
3.1400	2.9054	+0.0202	2.4298	2.3189	+0.0353
			2.6336	2.5227	+0.0304
			2.8444	2.7335	+0.0264
			3.1958	3.0849	+0.0230
			3.4770	3.3661	+0.0210

TABLE 3 (Continued)

x/L = 1.045	
r/r_{max}	C_p
0.0000	+0.0404
0.0562	+0.0444
0.1195	+0.0483
0.1687	+0.0518
0.2179	+0.0537
0.2811	+0.0562
0.3374	+0.0557
0.4076	+0.0552
0.4849	+0.0562
0.5552	+0.0547
0.6255	+0.0547
0.6888	+0.0517
0.7731	+0.0497
0.8715	+0.0472
0.9699	+0.0467
1.0823	+0.0427
1.1807	+0.0427
1.2932	+0.0387
1.3986	+0.0382
1.5040	+0.0370
1.6516	+0.0323
1.8625	+0.0298
2.0311	+0.0288
2.3474	+0.0253
2.6356	+0.0209

TABLE 4 – MEASURED MEAN AND TURBULENT VELOCITY CHARACTERISTICS

x/L = 0.704 r_0/r_{max} = 1.0000 tan α = 0.0000

$\frac{r-r_0}{r_{max}}$	$\frac{u_x}{U_0}$	$\frac{v_r}{U_0}$	$\frac{\sqrt{\overline{u'^2}}}{U_0}$	$\frac{\sqrt{\overline{v'^2}}}{U_0}$	$\frac{\sqrt{\overline{w'^2}}}{U_0}$	$100\,\frac{\overline{-u'v'}}{U_0^2}$	$\frac{\overline{-u'v'}}{q^2}$	$\frac{r-r_0}{\delta_r}$	$\frac{\varepsilon}{U_\delta \delta_p^*}$	$\frac{\ell}{\delta_r}$	$\frac{\ell}{\sqrt{(r_0+\delta_r)^2-r_0^2}}$
0.0236	0.695	-0.015	0.067	0.035	0.040	0.1085	0.148	0.1005	0.0064	0.0330	0.0106
0.0377	0.742	-0.018	0.064	0.036	0.042	0.1189	0.167	0.1605	0.0098	0.0480	0.0154
0.0482	0.751	-0.016	0.062	0.035	0.041	0.0951	0.140	0.2052	0.0097	0.0532	0.0170
0.0588	0.796	-0.020	0.061	0.035	0.041	0.0940	0.142	0.2503	0.0098	0.0542	0.0174
0.0728	0.824	-0.021	0.058	0.034	0.040	0.0906	0.147	0.3100	0.0107	0.0606	0.0194
0.0869	0.857	-0.021	0.055	0.035	0.038	0.0955	0.167	0.3700	0.0124	0.0681	0.0218
0.1009	0.880	-0.023	0.053	0.032	0.036	0.0805	0.157	0.4296	0.0125	0.0750	0.0240
0.1150	0.904	-0.023	0.049	0.031	0.033	0.0713	0.160	0.4896	0.0120	0.0761	0.0243
0.1431	0.950	-0.024	0.037	0.025	0.028	0.0434	0.158	0.6093	0.0086	0.0697	0.0223
0.1853	0.985	-0.026	0.020	0.017	0.017	0.0121	0.123	0.7889	0.0058	0.0895	0.0286
0.2310	0.995	-0.026	0.007	0.007	0.007	0.0004	0.026	0.9835	0.0006	0.0574	0.0184
0.3048	0.995	-0.025	0.003	0.003	0.004	0.0005					
0.3786	0.995	-0.025	0.003	0.003	0.003	0.0005					
0.4418	0.995	-0.026	0.003	0.002	0.003	0.0004					
0.5086	0.995	-0.026	0.003	0.002	0.002	0.0004					
0.6491	0.996	-0.026	0.003	0.002	0.002	0.0003					
0.7897	0.995	-0.024	0.003	0.003	0.002	0.0006					
0.8705	0.996	-0.025	0.003	0.002	0.002	0.0005					
1.0080	0.995	-0.025	0.003	0.003	0.002	0.0005					
1.3590	0.996	-0.024	0.003	0.003	0.002	0.0004					
1.8650	0.995	-0.022	0.002	0.002	0.004	0.0002					

$\frac{\delta_p^*}{r_{max}} = 0.0383$, $\frac{\delta_r^*}{r_{max}} = 0.0394$, $\frac{\delta_r}{r_{max}} = 0.231$

$\frac{\theta_p}{r_{max}} = 0.0212$, $\frac{\Lambda}{r_{max}^2} = 0.0229$, $\frac{U_\delta}{U_0} = 1.010$

TABLE 4 (Continued)

$x/L = 0.831 \quad r_0/r_{max} = 0.9756 \quad \tan\alpha = -0.1008$

$\frac{r-r_0}{r_{max}}$	$\frac{u_x}{U_0}$	$\frac{v_r}{U_0}$	$\frac{\sqrt{\overline{u'^2}}}{U_0}$	$\frac{\sqrt{\overline{v'^2}}}{U_0}$	$\frac{\sqrt{\overline{w'^2}}}{U_0}$	$100\,\frac{\overline{-u'v'}}{U_0^2}$	$\frac{\overline{-u'v'}}{q^2}$	$\frac{r-r_0}{\delta_r}$	$\frac{\varepsilon}{U_\delta \delta_p^*}$	$\frac{\ell}{\delta_r}$	$\frac{\ell}{\sqrt{(r_0+\delta_r)^2-r_0^2}}$
0.0218	0.825	-0.048	0.068	0.039	0.043	0.1177	0.148	0.0943	0.0027	0.0095	0.0031
0.0324	0.876	-0.053	0.066	0.039	0.044	0.1036	0.132	0.1402	0.0099	0.0375	0.0122
0.0499	0.910	-0.056	0.062	0.039	0.044	0.0971	0.134	0.2159	0.0181	0.0747	0.0243
0.0675	0.939	-0.058	0.060	0.036	0.041	0.0814	0.125	0.2920	0.0174	0.0745	0.0242
0.0780	0.957	-0.055	0.055	0.036	0.040	0.0771	0.129	0.3374	0.0154	0.0679	0.0221
0.0886	0.977	-0.055	0.054	0.035	0.039	0.0644	0.115	0.3833	0.0135	0.0651	0.0212
0.1132	1.007	-0.057	0.048	0.031	0.034	0.0482	0.108	0.4897	0.0135	0.0754	0.0246
0.1308	1.029	-0.056	0.043	0.029	0.030	0.0445	0.125	0.5658	0.0135	0.0782	0.0255
0.1624	1.059	-0.056	0.033	0.022	0.023	0.0242	0.115	0.7025	0.0114	0.0899	0.0293
0.3100	1.070	-0.045	0.005	0.003	0.004						
0.3873	1.065	-0.038	0.004	0.004	0.003						
0.4822	1.063	-0.034	0.006	0.003	0.003						
0.6473	1.046	-0.023	0.002	0.001	0.003						
0.8441	1.035	-0.017	0.004	0.002	0.003						
1.0128	1.030	-0.008	0.002	0.001	0.003						
1.1744	1.021	-0.003	0.005	0.002	0.003						
1.3677	1.017	0.004	0.005	0.003	0.003						
1.5469	1.015	0.004	0.005	0.002	0.004						

$$\frac{\delta_p^*}{r_{max}} = 0.0265, \quad \frac{\delta_r^*}{r_{max}} = 0.0270, \quad \frac{\delta_r}{r_{max}} = 0.240$$

$$\frac{\theta_p}{r_{max}} = 0.0133, \quad \frac{\Lambda}{r_{max}^2} = 0.0138, \quad \frac{U_\delta}{U_0} = 1.070$$

TABLE 4 (Continued)

$x/L = 0.873$ $\quad r_0/r_{max} = 0.7984$ $\quad \tan\alpha = -0.2944$

$\frac{r-r_0}{r_{max}}$	$\frac{u_x}{U_0}$	$\frac{v_r}{U_0}$	$\frac{\sqrt{\overline{u'^2}}}{U_0}$	$\frac{\sqrt{\overline{v'^2}}}{U_0}$	$\frac{\sqrt{\overline{w'^2}}}{U_0}$	$100\,\frac{\overline{-u'v'}}{U_0^2}$	$\frac{\overline{-u'v'}}{q^2}$	$\frac{r-r_0}{\delta_r}$	$\frac{\varepsilon}{U_\delta \delta_p^*}$	$\frac{\ell}{\delta_r}$	$\frac{\ell}{\sqrt{(r_0+\delta_r)^2-r_0^2}}$
0.0182	0.644	-0.140	0.064	0.040	0.046	0.1650	0.210	0.0609	0.0032	0.0115	0.0047
0.0309	0.705	-0.146	0.062	0.039	0.044	0.1620	0.220	0.1035	0.0047	0.0169	0.0069
0.0450	0.791	-0.159	0.060	0.038	0.042	0.1540	0.230	0.1506	0.0091	0.0330	0.0135
0.0731	0.843	-0.162	0.058	0.035	0.040	0.1480	0.240	0.2449	0.0162	0.0599	0.0245
0.0871	0.871	-0.160	0.057	0.034	0.039	0.1230	0.210	0.2918	0.0163	0.0660	0.0270
0.1082	0.885	-0.159	0.052	0.032	0.036	0.0820	0.160	0.3625	0.0138	0.0684	0.0280
0.1293	0.907	-0.155	0.048	0.029	0.034	0.0690	0.160	0.4331	0.0133	0.0721	0.0295
0.1436	0.924	-0.148	0.046	0.028	0.033	0.0620	0.160	0.4810	0.0124	0.0709	0.0290
0.1785	0.952	-0.136	0.041	0.025	0.028	0.0330	0.110	0.5980	0.0114	0.0890	0.0364
0.2347	0.973	-0.119	0.022	0.016	0.018	0.0070	0.070	0.7862	0.0043	0.0750	0.0306
0.2910	0.990	-0.107	0.007	0.005	0.006	0.0008	0.070	0.9748	0.0009	0.0467	0.0191
0.3472	0.994	-0.100	0.004	0.003	0.003	0.0006	0.160	1.1630	0.0008	0.0193	0.0079
0.3823	0.995	-0.097	0.003	0.003	0.003						
0.4315	1.007	-0.093	0.003	0.002	0.002						
0.5861	1.012	-0.086									
0.7197	1.013	-0.079									
0.9165	1.013	-0.067									
1.1273	1.013	-0.056									
1.5068	1.011	-0.037									
1.8301	1.008	-0.028									
2.0480	1.009	-0.023									

$$\frac{\delta_p^*}{r_{max}} = 0.0451, \quad \frac{\delta_r^*}{r_{max}} = 0.0389, \quad \frac{\delta_r}{r_{max}} = 0.321$$

$$\frac{\theta_p}{r_{max}} = 0.0245, \quad \frac{\Lambda}{r_{max}^2} = 0.0222 \quad \frac{U_\delta}{U_0} = 1.010$$

TABLE 4 (Continued)

$x/L = 0.909 \quad r_0/r_{max} = 0.5378 \quad \tan\alpha = -0.3681$

$\frac{r-r_0}{r_{max}}$	$\frac{u_x}{U_0}$	$\frac{v_r}{U_0}$	$\frac{\sqrt{\overline{u'^2}}}{U_0}$	$\frac{\sqrt{\overline{v'^2}}}{U_0}$	$\frac{\sqrt{\overline{w'^2}}}{U_0}$	$100\,\frac{\overline{-u'v'}}{U_0^2}$	$\frac{\overline{-u'v'}}{q^2}$	$\frac{r-r_0}{\delta_r}$	$\frac{\varepsilon}{U_\delta \delta_p^*}$	$\frac{\ell}{\delta_r}$	$\frac{\ell}{\sqrt{(r_0+\delta_r)^2-r_0^2}}$
0.0309	0.396	-0.106	0.060	0.039	0.045	0.1600	0.220	0.0688	0.0025	0.0130	0.0071
0.0590	0.537	-0.136	0.059	0.038	0.044	0.1570	0.230	0.1313	0.0044	0.0230	0.0125
0.0871	0.620	-0.151	0.057	0.038	0.043	0.1550	0.240	0.1938	0.0063	0.0331	0.0180
0.1082	0.664	-0.156	0.055	0.037	0.042	0.1390	0.230	0.2407	0.0072	0.0395	0.0215
0.1363	0.730	-0.162	0.053	0.035	0.040	0.1290	0.230	0.3033	0.0082	0.0468	0.0255
0.1715	0.767	-0.163	0.050	0.032	0.037	0.1050	0.210	0.3816	0.0084	0.0535	0.0291
0.1996	0.805	-0.163	0.048	0.030	0.035	0.0903	0.200	0.4441	0.0081	0.0555	0.0302
0.2312	0.841	-0.162	0.044	0.028	0.033	0.0707	0.190	0.5144	0.0075	0.0579	0.0315
0.2568	0.866	-0.161	0.040	0.026	0.031	0.0560	0.170	0.5691	0.0069	0.0592	0.0322
0.2910	0.896	-0.158	0.036	0.023	0.026	0.0267	0.110	0.6474	0.0042	0.0522	0.0284
0.3331	0.920	-0.151	0.028	0.016	0.018	0.0114	0.080	0.8194	0.0022	0.0426	0.0232
0.3683	0.941	-0.146	0.024	0.011	0.013	0.0040	0.050	0.9756	0.0011	0.0367	0.0200
0.4034	0.957	-0.139	0.012	0.006	0.009	0.0010	0.040	1.0539	0.0004	0.0276	0.0150
0.4385	0.959	-0.134									
0.4737	0.961	-0.130									
0.5088	0.964	-0.125									
0.6775	0.981	-0.108									
0.8673	0.991	-0.092									
1.2116	0.995	-0.066									
1.6509	1.001	-0.045									
2.1604	1.004	-0.031									

$$\frac{\delta_p^*}{r_{max}} = 0.0924, \quad \frac{\delta_r^*}{r_{max}} = 0.1003, \quad \frac{\delta_r}{r_{max}} = 0.449$$

$$\frac{\theta_p}{r_{max}} = 0.0508, \quad \frac{\Lambda}{r_{max}^2} = 0.0345, \quad \frac{U_\delta}{U_0} = 0.962$$

TABLE 4 (Continued)

$x/L = 0.951 \quad r_0/r_{max} = 0.2346 \quad \tan\alpha = -0.2952$

$\frac{r-r_0}{r_{max}}$	$\frac{u_x}{U_0}$	$\frac{v_r}{U_0}$	$\frac{\sqrt{u'^2}}{U_0}$	$\frac{\sqrt{v'^2}}{U_0}$	$\frac{\sqrt{w'^2}}{U_0}$	$100\,\frac{\overline{-u'v'}}{U_0^2}$	$\frac{\overline{-u'v'}}{q^2}$	$\frac{r-r_0}{\delta_r}$	$\frac{\varepsilon}{U_\delta \delta_p^*}$	$\frac{\ell}{\delta_r}$	$\frac{\ell}{\sqrt{(r_0+\delta_r)^2-r_0^2}}$
0.0236	0.251	-0.050	0.036	0.026	0.030	0.0443	0.154	0.0347	0.0004	0.0054	0.0041
0.0447	0.281	-0.053	0.041	0.028	0.032	0.0584	0.167	0.0657	0.0011	0.0127	0.0098
0.0588	0.297	-0.055	0.044	0.032	0.034	0.0775	0.191	0.0864	0.0015	0.0178	0.0137
0.0693	0.322	-0.059	0.045	0.032	0.035	0.0852	0.198	0.1018	0.0024	0.0219	0.0169
0.0869	0.345	-0.061	0.047	0.033	0.037	0.0830	0.178	0.1277	0.0026	0.0245	0.0188
0.1009	0.374	-0.064	0.048	0.035	0.038	0.0924	0.189	0.1482	0.0026	0.0226	0.0174
0.1220	0.413	-0.070	0.051	0.036	0.039	0.1053	0.194	0.1792	0.0027	0.0227	0.0174
0.1431	0.462	-0.077	0.052	0.036	0.041	0.0996	0.177	0.2102	0.0026	0.0223	0.0172
0.1712	0.511	-0.079	0.050	0.036	0.041	0.1077	0.190	0.2515	0.0029	0.0235	0.0181
0.2134	0.583	-0.082	0.049	0.036	0.041	0.0973	0.182	0.3135	0.0027	0.0234	0.0180
0.2275	0.612	-0.085	0.044	0.032	0.041	0.0744	0.161	0.3342	0.0024	0.0236	0.0182
0.2521	0.638	-0.087	0.044	0.031	0.040	0.0729	0.161	0.3703	0.0035	0.0349	0.0269
0.2766	0.667	-0.086	0.043	0.032	0.040	0.0791	0.179	0.4063	0.0038	0.0366	0.0282
0.2977	0.690	-0.085	0.042	0.030	0.039	0.0664	0.160	0.4373	0.0036	0.0369	0.0284
0.3329	0.723	-0.086	0.040	0.030	0.038	0.0672	0.170	0.4890	0.0041	0.0423	0.0326
0.3996	0.777	-0.083	0.038	0.029	0.034	0.0568	0.167	0.5870	0.0040	0.0446	0.0343
0.4734	0.833	-0.080	0.034	0.024	0.027	0.0436	0.175	0.6954	0.0027	0.0346	0.0268
0.5507	0.887	-0.077	0.023	0.015	0.016	0.0130	0.130	0.8090	0.0014	0.0331	0.0255
0.6421	0.913	-0.073	0.009	0.007	0.007	0.0001	0.003	0.9432	0.0000	0.0100	0.0078
0.7475	0.925	-0.062	0.004	0.003	0.003						
0.9233	0.931	-0.053	0.003	0.002	0.003						
1.0322	0.934	-0.047	0.003	0.002	0.002						
1.4539	0.950	-0.030	0.003	0.003	0.002						
1.8123	0.961	-0.022	0.003	0.001	0.002						
2.2024	0.963	-0.012	0.003	0.003	0.002						
2.6662	0.976	-0.002	0.003	0.002	0.002						

$\frac{\delta_p^*}{r_{max}} = 0.1952, \quad \frac{\delta_r^*}{r_{max}} = 0.2322, \quad \frac{\delta_r}{r_{max}} = 0.654$

$\frac{\theta_p}{r_{max}} = 0.1000, \quad \frac{\Lambda}{r_{max}^2} = 0.0480, \quad \frac{U_\delta}{U_0} = 0.935$

TABLE 4 (Continued)

x/L = 0.987 r_0/r_{max} = 0.1109 tan α = - 0.0899

$\frac{r-r_0}{r_{max}}$	$\frac{u_x}{U_0}$	$\frac{v_r}{U_0}$	$\frac{\sqrt{\overline{u'^2}}}{U_0}$	$\frac{\sqrt{\overline{v'^2}}}{U_0}$	$\frac{\sqrt{\overline{w'^2}}}{U_0}$	$100\ \frac{\overline{-u'v'}}{U_0^2}$	$\frac{\overline{-u'v'}}{q^2}$	$\frac{r-r_0}{\delta_r}$	$\frac{\varepsilon}{U_\delta \delta_p^*}$	$\frac{\ell}{\delta_r}$	$\frac{\ell}{\sqrt{(r_0+\delta_r)^2-r_0^2}}$
0.0182	0.365	-0.014	0.031	0.019	0.026	0.0132	0.065	0.0233	0.0001	0.0024	0.0021
0.0252	0.371	-0.016	0.031	0.022	0.026	0.0196	0.092	0.0324	0.0001	0.0144	0.0127
0.0322	0.378	-0.018	0.032	0.025	0.026	0.0227	0.098	0.0414	0.0010	0.0161	0.0142
0.0533	0.386	-0.021	0.035	0.026	0.028	0.0372	0.140	0.0684	0.0017	0.0206	0.0182
0.0604	0.395	-0.021	0.037	0.027	0.028	0.0410	0.135	0.0775	0.0019	0.0217	0.0191
0.0814	0.412	-0.025	0.041	0.030	0.031	0.0564	0.160	0.1045	0.0025	0.0254	0.0224
0.1025	0.434	-0.025	0.042	0.031	0.033	0.0633	0.168	0.1316	0.0029	0.0269	0.0238
0.1306	0.465	-0.026	0.049	0.032	0.035	0.0757	0.164	0.1677	0.0034	0.0294	0.0259
0.1482	0.487	-0.028	0.049	0.034	0.036	0.0890	0.185	0.1903	0.0039	0.0313	0.0276
0.1763	0.520	-0.028	0.050	0.035	0.037	0.0871	0.171	0.2263	0.0038	0.0307	0.0271
0.2290	0.593	-0.030	0.052	0.033	0.036	0.0828	0.164	0.2940	0.0036	0.0294	0.0260
0.2853	0.655	-0.031	0.046	0.030	0.036	0.0629	0.147	0.3662	0.0032	0.0305	0.0269
0.3520	0.721	-0.030	0.042	0.029	0.035	0.0541	0.141	0.4549	0.0032	0.0325	0.0287
0.4610	0.809	-0.031	0.038	0.027	0.033	0.0524	0.161	0.5918	0.0042	0.0432	0.0381
0.5383	0.855	-0.029	0.035	0.025	0.029	0.0421	0.158	0.6910	0.0037	0.0431	0.0380
0.6085	0.899	-0.028	0.029	0.019	0.021	0.0224	0.135	0.7811	0.0023	0.0370	0.0326
0.6823	0.929	-0.025	0.015	0.011	0.013	0.0056	0.109	0.8759	0.0011	0.0359	0.0317
0.7456	0.938	-0.025	0.006	0.005	0.009						
0.8124	0.941	-0.022	0.004	0.004	0.006						
0.8897	0.946	-0.020	0.003	0.003	0.003						
1.0583	0.955	-0.017	0.006	0.003	0.003						
1.2305	0.959	-0.013	0.005	0.003	0.003						
1.5890	0.961	-0.006	0.004	0.004	0.003						
1.9369	0.971	-0.001	0.004	0.003	0.003						
2.3094	0.977	0.001	0.004	0.003	0.004						
2.6397	0.977	0.008	0.004	0.003	0.004						
2.8013	0.979	0.010	0.004	0.004	0.004						

$\frac{\delta_p^*}{r_{max}} = 0.1960$, $\frac{\delta_r^*}{r_{max}} = 0.2575$, $\frac{\delta_r}{r_{max}} = 0.745$

$\frac{\theta_p}{r_{max}} = 0.1103$, $\frac{\Lambda}{r_{max}^2} = 0.0403$, $\frac{U_\delta}{U_0} = 0.942$

measured by the single-element probe are presented in the figures along with the values measured by the two-component probe.

THEORY

The Douglas C-S method[5] solves the standard incompressible, steady continuity and momentum equations for thin axisymmetric boundary layers. This set of partial differential equations, with the addition of the transverse curvature effects, is

$$\frac{\partial(ru_s)}{\partial s} + \frac{\partial(rv_n)}{\partial n} = 0 \tag{5}$$

and

$$u_s \frac{\partial u_s}{\partial s} + v_n \frac{\partial u_s}{\partial n} = -\frac{1}{\rho}\frac{dp}{ds} + \frac{1}{r}\frac{\partial}{\partial n}\left[r\left(\nu \frac{\partial u_s}{\partial n} - \overline{u_s' v_n'}\right)\right] \tag{6}$$

where u_s = mean velocity component in the s direction (parallel to the body meridian)

v_n = mean velocity component in the n direction (normal to the body meridian)

p = pressure on the body

r = $r_0(s,n) + n \cos \alpha$

r_0 = body radius

x = axial distance measured from the nose

ν = kinematic viscosity of the fluid

$\overline{u_s' v_n'}$ = Reynolds stress

u_s' = velocity fluctuation in the s direction

v_n' = velocity fluctuation in the n direction

The wall boundary conditions are $u_s(s,n) = v_n(s,n) = 0$ at $n = 0$. Effects due to longitudinal curvature are neglected. The Reynolds stress model is given in detail in the section presenting the turbulence characteristics.

The Reynolds stress $-\overline{u'_s v'_n}$ in the modified Douglas C-S computer code is modeled[1,5,13] by

$$-\overline{u'_s v'_n} = \begin{cases} \varepsilon_i \\ \\ \varepsilon_0 \end{cases} \frac{\partial u_s}{\partial n} \qquad \begin{matrix} \text{for } 0 \leq n \leq n_c \\ \\ \text{for } n_c \leq n \leq \delta \end{matrix} \tag{7}$$

where $\varepsilon_i = \ell^2 \left(\frac{r}{r_0}\right) \frac{\partial u_s}{\partial n}$ = eddy viscosity in the inner region

$\varepsilon_0 = 0.0168\, U_e\, \delta_p^*\, \gamma_{tr}$ = eddy viscosity in the outer region

$\ell = 0.4\, r_0 \ln\left(\frac{r}{r_0}\right)\left\{1 - \exp\left[-\frac{r_0}{A} \ln\left(\frac{r}{r_0}\right)\right]\right\}$ = mixing length parameter in the inner region

$A = 26\, \nu \left(\frac{\tau_w}{\rho}\right)^{-1/2}$ = Van Driest's damping factor

$\delta = \delta_{0.995}$ = boundary layer thickness $\frac{u_s}{U_e} = 0.995$

$\delta_p^* = \int_0^{\delta} \left(1 - \frac{u_s}{U_e}\right) dn$ = planar displacement thickness

U_e = computed potential flow velocity at the edge of the displacement body

τ_w = wall shear stress

n_c = value of n at which $\varepsilon_i = \varepsilon_0$

The Douglas C-S computer code is used to calculate the velocity components u_s and v_n parallel to and normal to the body surface, respectively. Wang and Huang[3] modified these velocity components by using the predicted potential flow velocities outside of the displacement body and converted the normal and tangential velocity components to axial and radial components for comparison with the experimental values.

COMPARISON OF MEAN PROFILES

Figure 7 shows a comparison of the theoretically predicted and experimentally measured mean axial u_x and radial v_r velocity profiles at various axial locations on the body. The velocity components are nondimensionalized by the free stream velocity U_0. The solid curves represent the theoretical results, the open symbols are the "X" hot-film values, and the solid symbols are the single element hot-wire values. The accuracies of the experimental measurements of u_x/U_0 and v_r/U_0 were estimated to be about 0.5 percent and 1.0 percent, respectively.

Figure 7 shows the good agreement between the theoretical and the "X" hot-film experimental axial velocity profiles, and even better agreement with the theory for the single element sensor. Wang and Huang[3] modified the eddy viscosity model, and this modeling plays an important role in computations of axial velocity profiles near the wall. The agreement between theory and experiment is shown in Figure 7 to be very satisfactory near the wall.

The agreement between theory and experiment for the radial velocity profiles is generally less satisfactory. This velocity component is small and more difficult to measure accurately. Nevertheless, the maximum difference between the computed and measured values of v_r/U_0 is less than 0.03.

COMPARISON OF MEASURED AND COMPUTED INTEGRAL PARAMETERS

The distributions of (radial) displacement thickness δ_r^* and (radial) boundary layer thickness δ_r are given in Figure 8 along with the stern profile of the axisymmetric body. The theoretical boundary layer thickness

Figure 7 - Computed and Measured Mean Axial and Radial Velocity Distribution Across Stern Boundary Layer of Afterbody 5

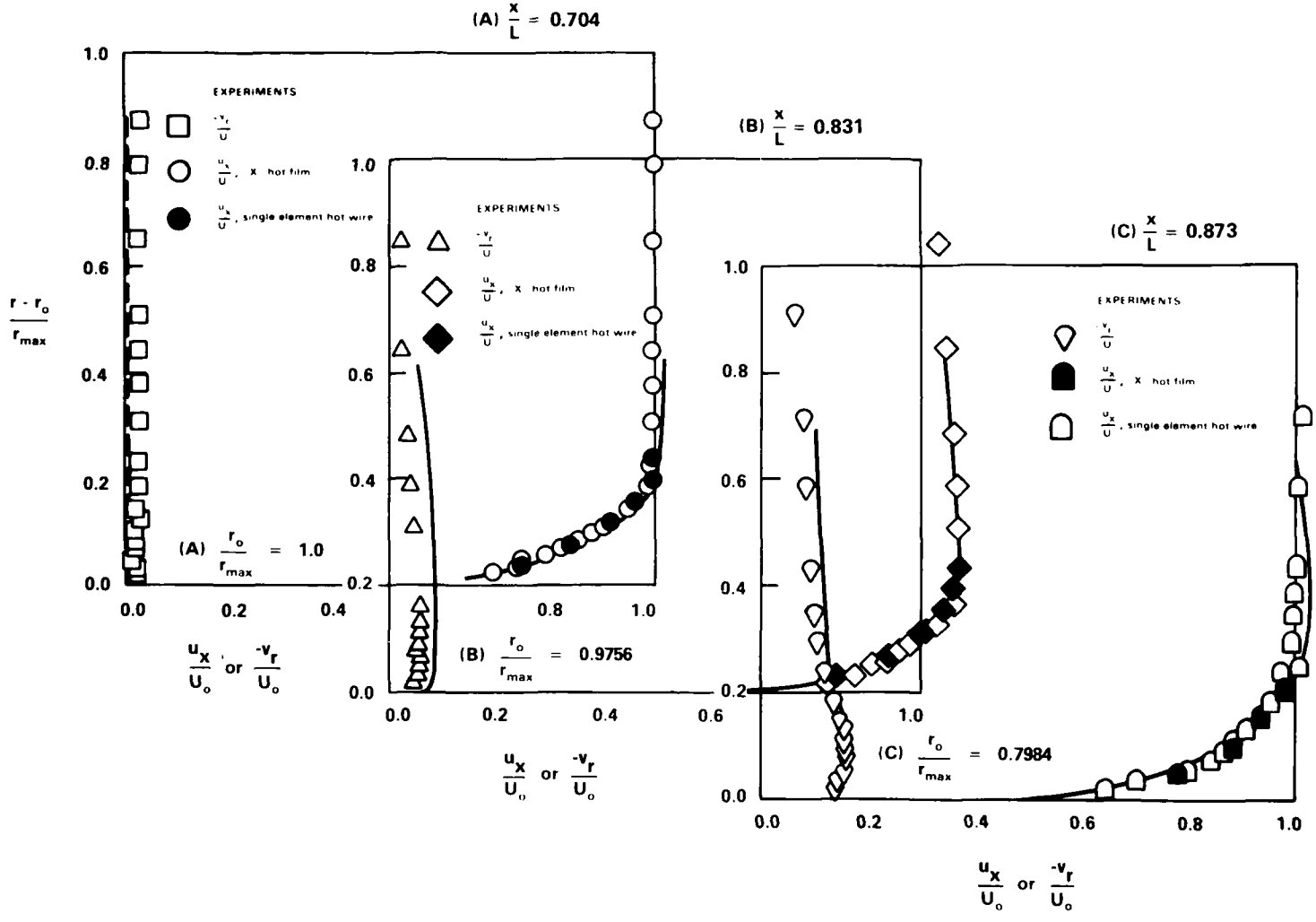

Figure 7a - Nondimensional Axial Lengths, x/L = 0.704, 0.831, 0.873

Figure 7 (Continued)

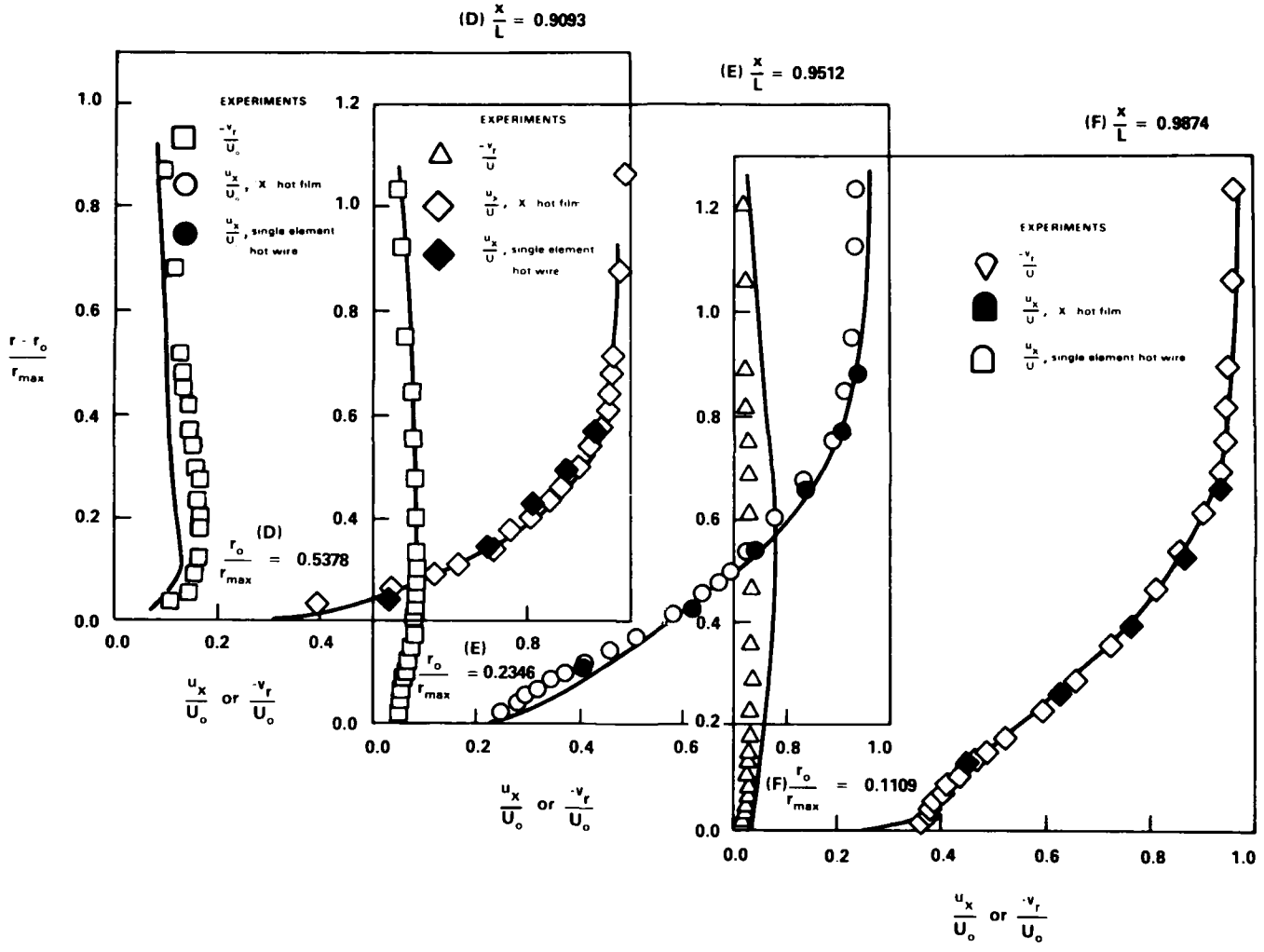

Figure 7b - Nondimensional Axial Lengths, x/L = 0.909, 0.951, 0.987

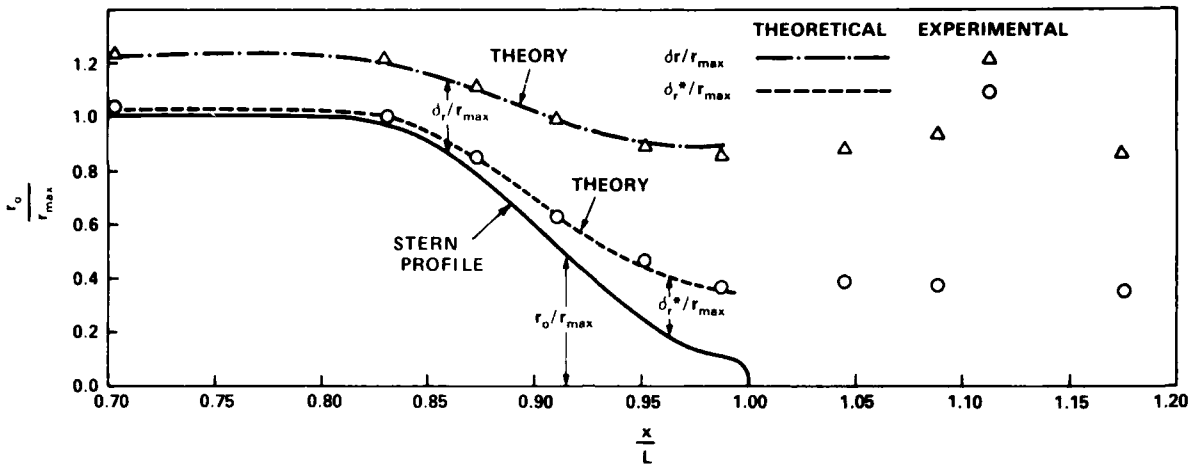

Figure 8 - Comparison of Measured and Computed Boundary Layer and Displacement Thickness Parameters

is defined as the normal distance from the body where the nondimensionalized tangential velocity u_s/U_e has a value of 0.995. In this definition, u_s is the dimensional tangential velocity and U_e is the dimensional local tangential velocity calculated by the potential flow program using the latest body-wake displacement model.

The measured value of the boundary layer thickness δ_r is a difficult value to obtain. This variable is defined as the radial position where Reynolds stress $\overline{u'_x v'_r}$ becomes "small." The overall accuracy of the measured values of δ_r presented in the present investigation is estimated to be about 10 percent.

The integral parameters of interest are:[1]

$$\frac{\delta_p^*}{r_{max}} = \int_{r_0/r_{max}}^{(r_0+\delta_r)/r_{max}} \left(1 - \frac{u_x}{U_\delta}\right) d\left(\frac{r}{r_{max}}\right) \tag{8}$$

$$\frac{\Lambda}{r_{max}^2} = \int_{r_0/r_{max}}^{(r_0+\delta_r)/r_{max}} \left(1 - \frac{u_x}{U_\delta}\right)\left(\frac{r}{r_{max}}\right) d\left(\frac{r}{r_{max}}\right) \tag{9}$$

$$\frac{\delta_r^*}{r_{max}} = \sqrt{\left(\frac{r_0}{r_{max}}\right)^2 + 2\,\frac{\Lambda}{r_{max}^2}} - \frac{r_0}{r_{max}} \tag{10}$$

$$\frac{\theta_p}{r_{max}} = \int_{r_0/r_{max}}^{(r_0+\delta_r)/r_{max}} \left(1 - \frac{u_x}{U_\delta}\right)\frac{u_x}{U_\delta}\, d\left(\frac{r}{r_{max}}\right) \tag{11}$$

$$\frac{\Omega}{r_{max}^2} = \int_{r_0/r_{max}}^{(r_0+\delta_r)/r_{max}} \left(1 - \frac{u_x}{U_\delta}\right)\left(\frac{u_x}{U_\delta}\right)\left(\frac{r}{r_{max}}\right) d\left(\frac{r}{r_{max}}\right) \tag{12}$$

where U_δ is the value of u_x at $r = r_0 + \delta_r = r_0 + n_\delta \sec \alpha$ and n_δ is the value of boundary-layer thickness measured normal to the body surface. The values of integral parameters derived from the measured axial velocity profiles, u_x/U_δ, are given in Table 4. Figure 8 shows the theoretical and measured values of (radial) boundary-layer thickness δ_r and the (radial) displacement thickness δ_r^*. The agreement between measured and computed values of δ_r and δ_r^* is satisfactory.

MEASURED TURBULENCE CHARACTERISTICS

The cross-wire probe was used to measure the turbulence characteristics in the thick boundary layer. The measured Reynolds stresses and the measured mean velocity profiles were used to obtain eddy viscosity and mixing length.

MEASURED REYNOLDS STRESSES

The exchange of momentum in the turbulent mixing process is represented by the distribution of the Reynolds stresses $-\overline{u'v'}$, $\overline{u'^2}$, $\overline{v'^2}$, and $\overline{w'^2}$ where $\overline{u'^2}$, $\overline{v'^2}$, and $\overline{w'^2}$ are the turbulent fluctuations in the axial,

radial, and azimuthal directions, respectively. With the probe elements alined vertically, the Reynolds stress and the axial and radial fluctuations are computed by an on-line computer with a sampling rating of 1024 data values in 8 seconds. To obtain the azimuthal fluctuation $\overline{w'^2}$, the hot film sensor is rotated 90 degrees. Data points are accepted at the same rate and analyzed by the same computer.

Figure 9 shows the nondimensionalized measured distributions of Reynolds stress $-\overline{u'v'}/U_0^2$ and the three components of turbulent fluctuations $\sqrt{\overline{u'^2}}/U_0$, $\sqrt{\overline{v'^2}}/U_0$, and $\sqrt{\overline{w'^2}}/U_0$ at various axial locations along the axisymmetric body. The axial fluctuation component is the largest of the three components for all axial locations. The radial velocity fluctuation component has the smallest value. The intensity of each of the three components is larger near the surface of the stern and reduces as the boundary-layer thickens for $x/L < 0.95$. A sharp gradient exists in the turbulence velocity components near the surface since velocities go to zero at the wall.

The maximum value of the nondimensionalized Reynolds stress $-\overline{u'v'}/U_0^2$ occurs near the wall for $x/L < 0.873$ with a strong variation in the radial direction.* As the axial location increases and the boundary layer thickends, the radial location of maximum Reynolds stress moves away from the wall. The Reynolds stress reduces quickly from the maximum value to zero at the edge of the boundary layer. At axial locations of $x/L = 0.951$ and 0.987, the measured values of $-\overline{u'v'}$ reduce from the maximum value to zero at the wall. These results are consistent with those of Huang et al.[1] for the two afterbody shapes tested.

Huang et al.[1] also have presented measured distributions of a turbulence structure parameter a_1 where $a_1 = -\overline{u'v'}/q^2$ and $q^2 = \overline{u'^2} + \overline{v'^2} + \overline{w'^2}$. Thin boundary layer data show a_1 to have a constant value of approximately 0.15 between 0.05δ and 0.8δ. The data of Huang et al.[1] indicated that for a thick axisymmetric boundary layer, a_1 had a value of approximately 0.16

*The spatial resolution of the "X" hot-film probe used may not be fine enough to measure the Reynolds stresses precisely near the wall of the thin boundary layer.

Figure 9 - Measured Distributions of Reynolds Stresses for Afterbody 5

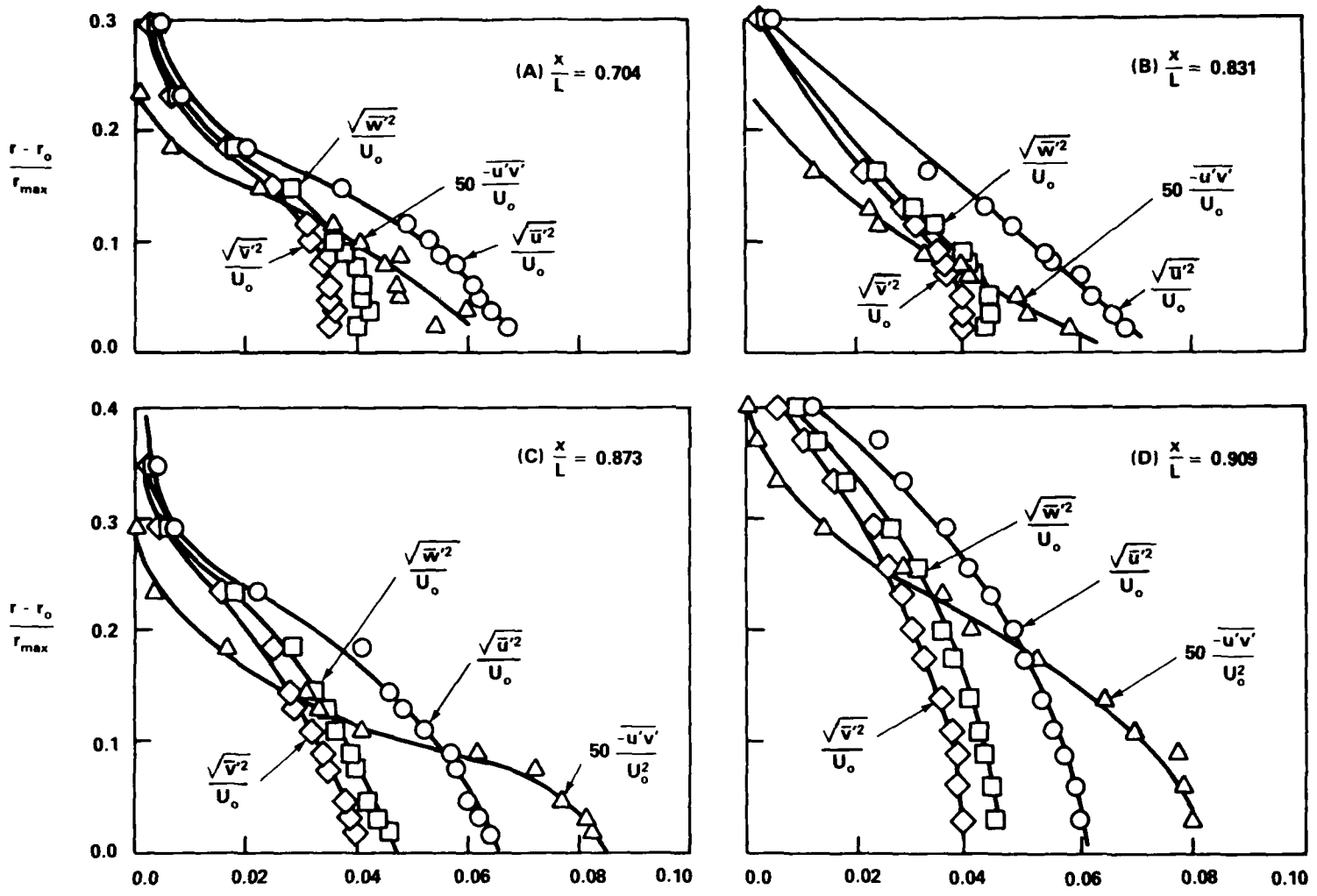

Figure 9a - Nondimensional Axial Lengths, x/L = 0.704, 0.831, 0.873, 0.909

Figure 9 (Continued)

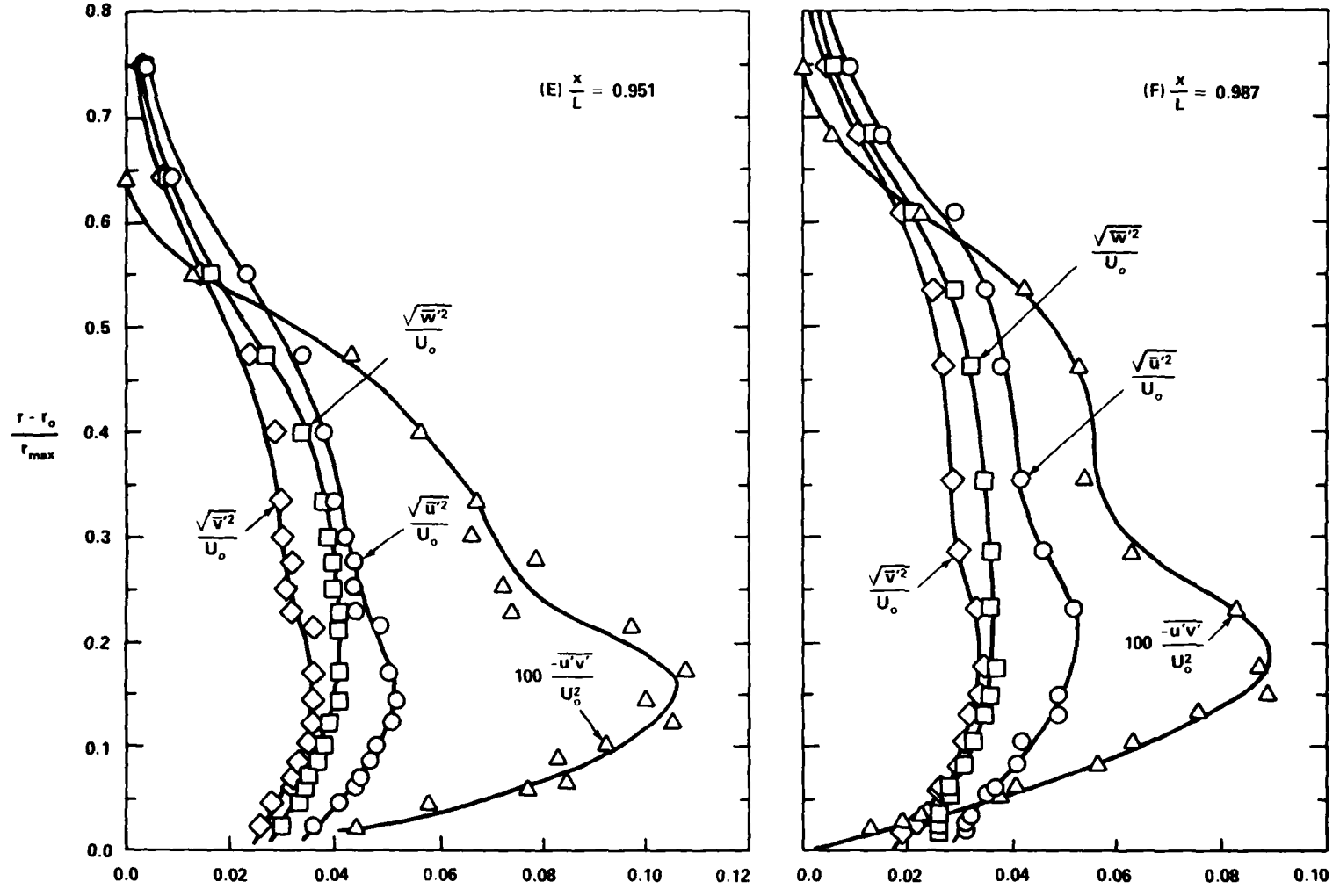

Figure 9b - Nondimensional Axial Lengths, x/L = 0.951, 0.987

up to $(r-r_0)/\delta_r = 0.6$, and that the value of a_1 decreased toward the edge of the boundary layer. The values of a_1 measured on the present axisymmetric body are shown in Figure 10. The present results are similar to the earlier results of Huang et al.[1] The values of a_1 decrease in the inner region at the location of $x/L = 0.987$.

No attempt was made to remove the free-stream turbulence fluctuations from the measured components of turbulence velocities. The reduction in the value of a_1 near the edge of the boundary layer is in part caused by the larger contribution of the free-stream turbulence to q^2 than to $-\overline{u'v'}$ (Reference 1).

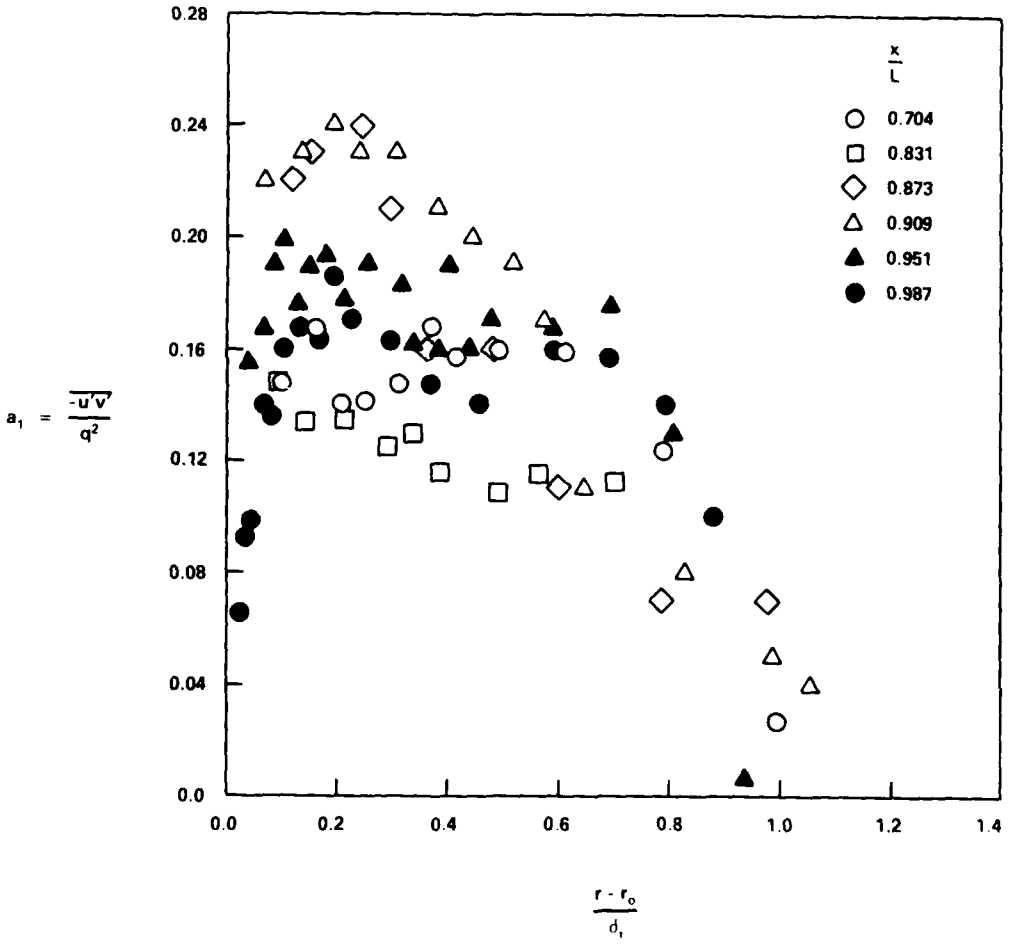

Figure 10 - Measured Distributions of Turbulent Structure Parameter

EDDY VISCOSITY AND MIXING LENGTH

The experimental values of eddy viscosity ε and mixing length ℓ across the thick stern boundary layer are derived from the measured values of Reynolds stress $-\overline{u'v'}$ and the mean velocity gradient $\frac{\partial u_x}{\partial r}$, using the definitions[1,5,13]

$$-\overline{u'v'} = \varepsilon \frac{\partial u_x}{\partial r} \tag{13}$$

and

$$-\overline{u'v'} = \ell^2 \left|\frac{\partial u_x}{\partial r}\right| \frac{\partial u_x}{\partial r} \tag{14}$$

where the Reynolds stress $-\overline{u'v'}$ and the axial velocity u_x are measured by the "X" hot-film probe. By fairing the measured velocity profile u_x with a 'spline' curve, the value of $\partial u_x/\partial_r$ can be computed numerically.

The experimentally-determined distributions of eddy viscosity $\varepsilon/U_\delta\ \delta_p^*$ are given in Figure 11 for the axisymmetric body under consideration. The

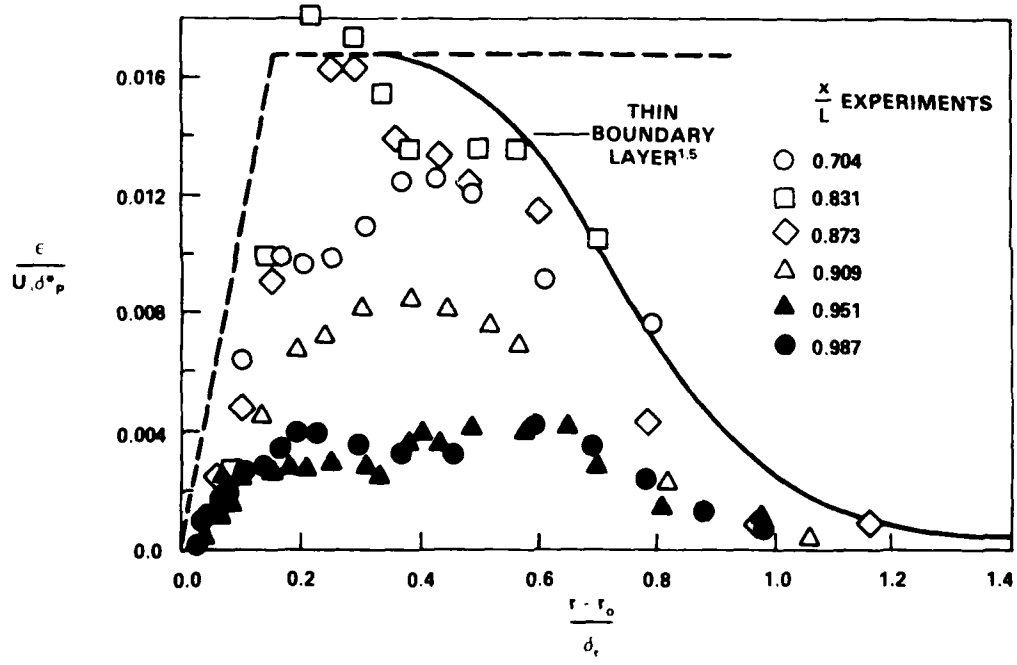

Figure 11 - Measured Distributions of Eddy Viscosity for Afterbody 5

solid curve in this figure is the thin boundary layer eddy-viscosity model of Cebeci and Smith.[5] The experimental values of eddy viscosity for axial locations, $x/L \leq 0.873$, where the boundary layer is thin, agree reasonably well with the Cebeci and Smith model. However, as the boundary layer thickens, the measured values of $\varepsilon/U_\delta \delta_p^*$ become nearly one-fifth of the values for thin boundary layers given by the Cebeci and Smith model.[5]

The experimentally-determined distributions of mixing length ℓ/δ_r are shown in Figure 12. The solid curve in this figure gives the thin boundary layer results of Bradshaw, Ferriss, and Atwell.[13] Again, agreement is reasonable for $x/L \leq 0.873$ and the experimental values in the thicker boundary layers are roughly one-third the values in the thin boundary layers. Similar reductions of eddy viscosity and mixing length also were measured earlier by Huang et al.[1] and by Patel and Lee.[9] The experimentally-derived eddy-viscosity and mixing-length data are also given in Table 4.

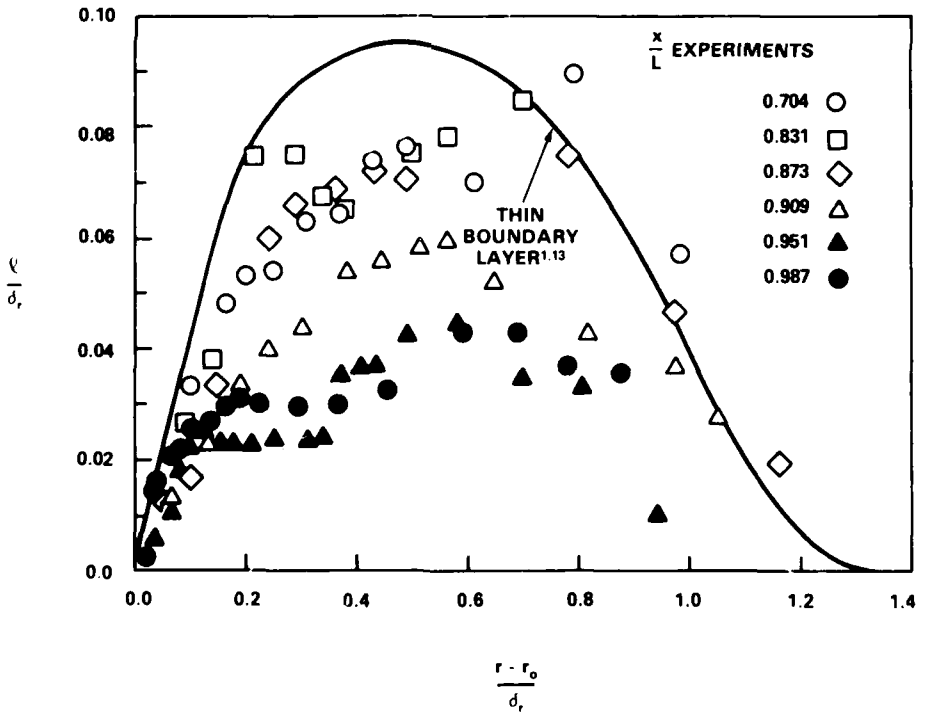

Figure 12 - Measured Distributions of Mixing Length for Afterbody 5

TURBULENCE MODEL

Figure 12 shows that the distribution of measured mixing length in the thin boundary layer is roughly approximated by the thin boundary layer results of Bradshaw et al.[13] However, the thick boundary layer values of ℓ/δ_r are considerably smaller than Bradshaw's thin boundary layer results. Figure 12 also shows that the maximum values of the mixing length occur at approximately the same radial location for theory and experiment. Huang et al.[1] proposed that the mixing length of an axisymmetric turbulent boundary layer is proportional to the square root of the entire turbulence annulus between the body surface and the edge of the boundary layer

$$\ell \sim \sqrt{(r_0+\delta_r)^2-r_0^2} \tag{15}$$

The present measured values of $\ell/\sqrt{(r_0+\delta_r)^2-r_0^2}$ are given in Figure 13 where the solid curve is derived by Huang et al.[1] This figure shows that the values measured agree reasonably well with Huang's hypothesis.

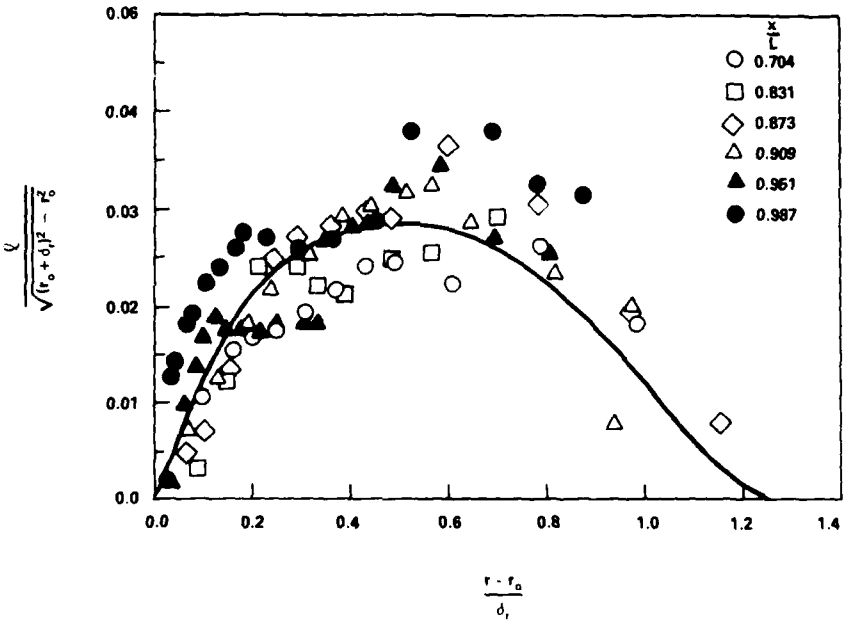

Figure 13 - Similarity Concept for Mixing Length of Thick Axisymmetric Stern Turbulent Boundary Layer

The new mixing length definition has been incorporated into the Douglas C-S boundary layer method of Wang and Huang.[3] The original mixing length formulation is approximately valid and is used until the boundary layer thickness is greater than 20 percent of the body radius ($\delta_r > 0.2\ r_0$). At this point, the boundary layer is considered thick and the mixing length ℓ is defined by

$$\ell = \ell_0 \frac{\sqrt{(r_0+\delta_r)^2 - r_0^2}}{3.31\ \delta_r} \tag{16}$$

Huang derived this equation and the limits on its use from the maximum values of mixing length given by Bradshaw,[13] ℓ_0, and the experimental data of Huang et al.[1]

TURBULENCE REYNOLDS NUMBER

The axial turbulence velocity Reynolds number is defined as

$$R_\lambda = \frac{\sqrt{\overline{u_x'^2}}\ \lambda}{\nu} \tag{17}$$

where λ is the microscale of the turbulence computed by the relationship

$$\lambda^2 = \frac{\overline{u_x'^2}\ \overline{u_x^2}}{\overline{\left(\frac{\partial u_x'}{\partial t}\right)^2}} \tag{18}$$

Here, Taylor's hypothesis, the assumption of an isotropic field of turbulence (although not quite true in Figure 10) and space-time equivalence, is used to obtain the microscale λ. The time differentiation of u_x' was accomplished by using an analog operational amplifier (as used by Frenkiel et al.[14]) in a differentiating mode. The departure from linearity as a

function of frequency was found to be 1 percent at 10 kHz and 5 percent at 20 kHz. The axial velocity fluctuation u_x' was recorded on magnetic tape for 30 sec at a tape speed of 152.4 cm/s using a multichannel recorder. This tape recorder had a rapid fall-off in response above 20 kHz. The recorded data for u_x' were played back to determine the mean square values of $\overline{u_x'^2}$ and $\overline{(\partial u_x'/\partial t)^2}$ (with the signal passing through the differentiation amplifier) by a true RMS voltmeter.

The measured values of turbulence Reynolds number R_λ at various axial locations of Afterbody 5 are shown in Figure 14. The value of R_λ decreases

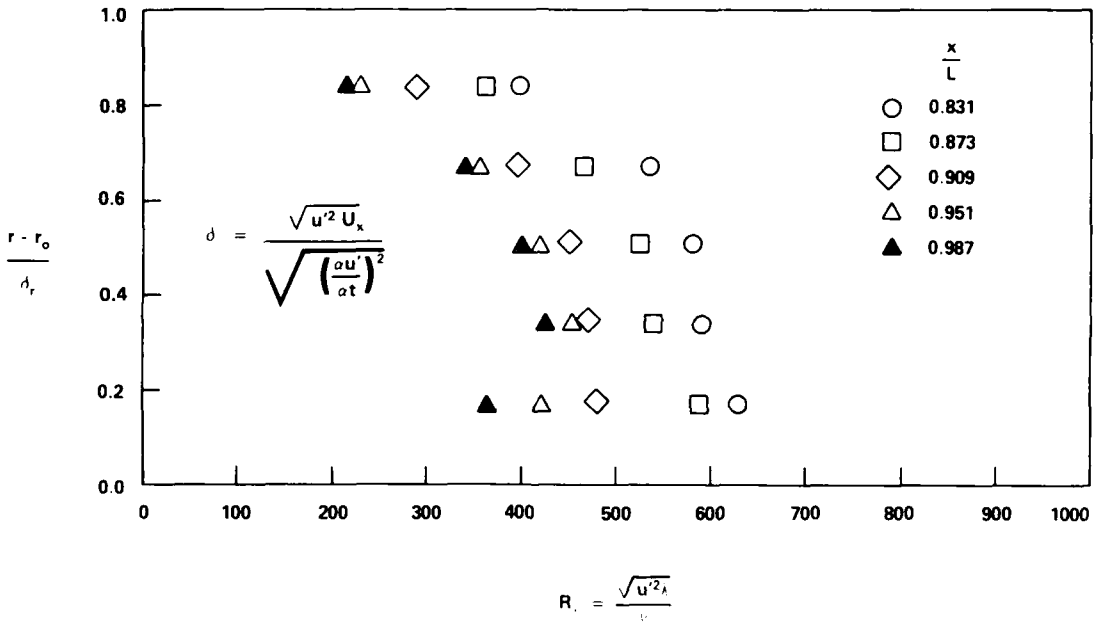

Figure 14 - Measured Turbulent Reynolds Numbers

with increasing axial distance x, which is a distinguishing characteristic of a thick stern boundary layer. For a given x/L, the measured values of R_λ are almost constant for distances less than 60 percent of the boundary layer thickness. The measured values of R_λ in this thick stern boundary layer are higher than those generated by most turbulence grids.[14] The turbulence Reynolds number R_λ in the present thick stern boundary layer is

sufficiently high that the results obtained should be typical of high Reynolds number thick stern turbulent boundary layer flows.

TURBULENT LENGTH SCALE IN THICK STERN BOUNDARY LAYER

The experimentally derived mixing length data in the thick stern boundary layers of Afterbodies 1, 2, and 5 indicate that the mixing-length scale is proportional to the square root of the annular area between the body surface and the edge of the boundary layer. It is of fundamental interest to perform an independent and more direct measurement of the turbulence length scale to support this empirical result. The spatial correlation coefficient of two axial velocity fluctuations at points A and B, $\rho_{AB}(d_r) = \overline{u'_A u'_B}/(\sqrt{\overline{u'^2_A}}\ \sqrt{\overline{u'^2_B}})$, as a function of the radial separation distance between the points A and B, $d_r = r_B - r_A$, is chosen for this purpose. The axial velocities at points A and B were measured by positioning two single-element TSI (Model 1212) hot-wire probes with 90-deg bends at the two points. The linearized outputs of the velocities from the two-channel TSI (Model 1050-1) hot-wire anemometer were a.c. coupled by using an amplifier with low frequency rolloff set at 1 Hz. The fluctuating velocity correlation $\overline{u'_A u'_B}$ was then measured by a TSI Correlator (Model 1015C). The spatial correlation coefficients were measured at various axial locations in the thick stern boundary layer of Afterbody 5. At each axial location, point A was fixed at $r_A = r_0 + 0.167\ \delta_r$ and the radial location ($r_B > r_A$) of point B was increased until the value of ρ_{AB} became "small."

The measured spatial correlation coefficients are plotted in Figure 15 (data are tabulated in Table 5) against three nondimensional length parameters, namely, $\eta = d_r/\sqrt{(r_0+d_r)^2-r_0^2}$, d_r/δ_r, and d_r/δ_p^*. As shown in Figure 15, the measured correlation coefficients at various axial locations are not similar when η is taken to be d_r/δ_r or d_r/δ_p^*; the correlation length scale of the turbulence in the thick stern boundary layer is not proportional to the local radial boundary-layer thickness δ_r or the planar displacement thickness δ_p^*. However, it is interesting to note that the

Figure 15 - Similarity Length Scale in Thick Axisymmetric Stern Boundary Layer

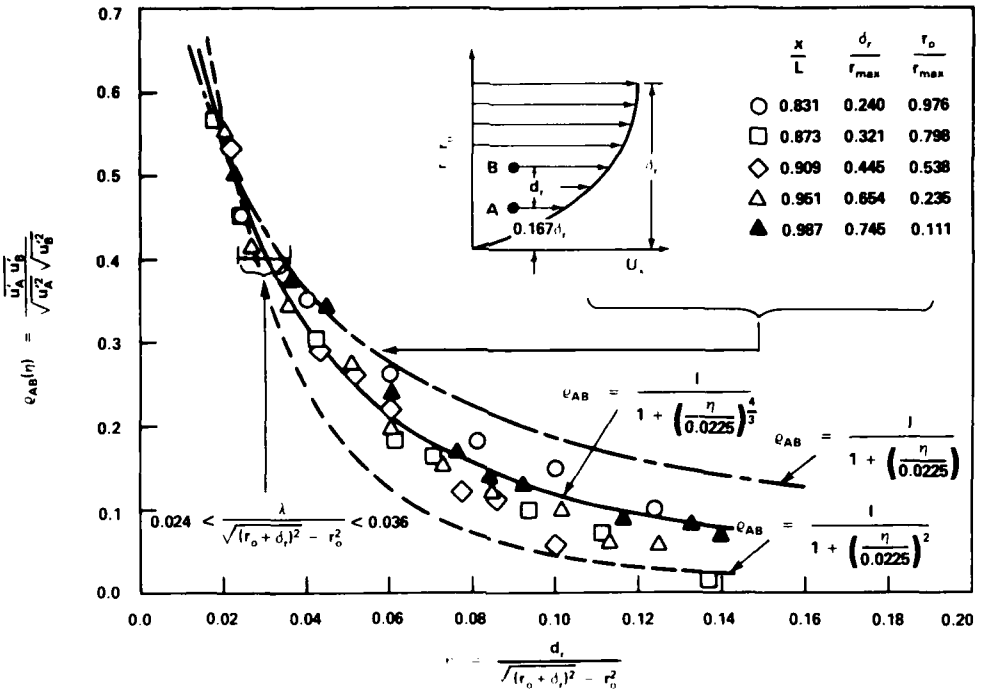

Figure 15a - Nondimensionalized by Turbulent Annular Area

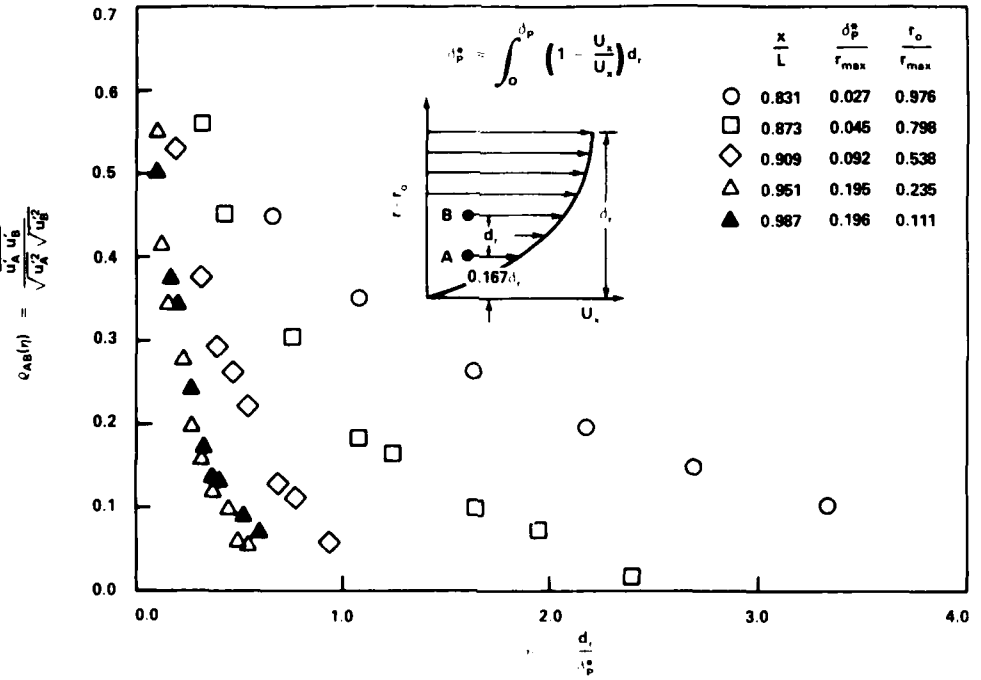

Figure 15b - Nondimensionalized by Planar Displacement Thickness

Figure 15 (Continued)

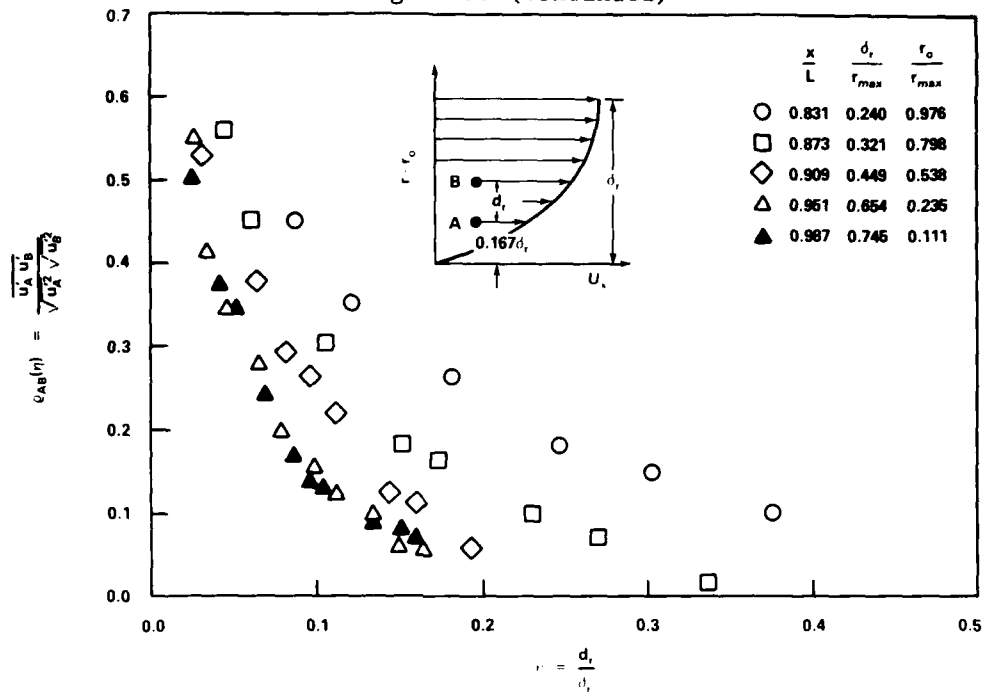

Figure 15c - Nondimensionalized by Boundary Layer Thickness

measured correlation coefficients at various axial locations in the thick stern boundary layer do possess a similarity form when the nondimensional length parameter η is taken to be $d_r/\sqrt{(r_0+\delta_r)^2-r_0^2}$. This independent and more direct measurement of the turbulence length scale as determined from the spatial correlation coefficient measurements provides additional support that the appropriate length scale in the thick axisymmetric stern boundary layer is proportional to the square root of the turbulence annular area between the body surface and the edge of the boundary layer. Throughout the entire stern boundary layer, the measured Taylor microscale λ at each axial location is found to be approximately equal to the measured correlation length scale d_r for which the measured correlation coefficient $\rho_{AB}(d_r)$ is equal to 0.4 (Figure 15). The measured values of $\lambda/\sqrt{(r_0+\delta_r)^2-r_0^2}$ were found to vary from 0.024 to 0.036 for the five axial locations (Figure 15). This is additional evidence of the similarity

TABLE 5 - MEASURED SPATIAL CORRELATION FUNCTIONS

$\frac{x}{L} = 0.831$, $\frac{r_0}{r_{max}} = 0.976$; $\frac{\delta_r}{r_{max}} = 0.240$, $\frac{\delta_p^*}{r_{max}} = 0.027$				$\frac{x}{L} = 0.873$, $\frac{r_0}{r_{max}} = 0.798$; $\frac{\delta_r}{r_{max}} = 0.321$, $\frac{\delta_p^*}{r_{max}} = 0.045$				$\frac{x}{L} = 0.909$, $\frac{r_0}{r_{max}} = 0.538$; $\frac{\delta_r}{r_{max}} = 0.445$, $\frac{\delta_p^*}{r_{max}} = 0.092$			
$\frac{d_r}{\sqrt{(r_0+\delta_r)^2-r_0^2}}$	$\frac{d_r}{\delta_p^*}$	$\frac{d_r}{\delta_r}$	ρ_{AB}	$\frac{d_r}{\sqrt{(r_c+\delta_r)^2-r_0^2}}$	$\frac{d_r}{\delta_p^*}$	$\frac{d_r}{\delta_r}$	ρ_{AB}	$\frac{d_r}{\sqrt{(r_0+\delta_r)^2-r_0^2}}$	$\frac{d_r}{\delta_p^*}$	$\frac{d_r}{\delta_r}$	ρ_{AB}
0.0245	0.658	0.074	0.450	0.0180	0.314	0.044	0.560	0.0220	0.197	0.0407	0.530
0.0400	1.075	0.121	0.350	0.0246	0.429	0.0601	0.450	0.0350	0.313	0.0647	0.379
0.0600	1.612	0.181	0.262	0.0428	0.746	0.105	0.303	0.0435	0.389	0.0804	0.291
0.0810	2.176	0.245	0.180	0.0618	1.077	0.151	0.181	0.0522	0.467	0.0965	0.263
0.100	2.686	0.302	0.147	0.0709	1.236	0.173	0.162	0.0606	0.542	0.112	0.219
0.124	3.331	0.375	0.100	0.0941	1.640	0.230	0.097	0.0775	0.693	0.143	0.122
				0.1115	1.944	0.272	0.070	0.0864	0.773	0.160	0.112
				0.1375	2.397	0.336	0.015	0.1050	0.939	0.194	0.056

$\frac{x}{L} = 0.951$, $\frac{r_0}{r_{max}} = 0.235$; $\frac{\delta_r}{r_{max}} = 0.654$, $\frac{\delta_p^*}{r_{max}} = 0.195$				$\frac{x}{L} = 0.987$, $\frac{r_0}{r_{max}} = 0.111$; $\frac{\delta_r}{r_{max}} = 0.745$, $\frac{\delta_p^*}{r_{max}} = 0.196$			
$\frac{d_r}{\sqrt{(r_0+\delta_r)^2-r_0^2}}$	$\frac{d_r}{\delta_p^*}$	$\frac{d_r}{\delta_r}$	ρ_{AB}	$\frac{d_r}{\sqrt{(r_0+\delta_r)^2-r_0^2}}$	$\frac{d_r}{\delta_p^*}$	$\frac{d_r}{\delta_r}$	ρ_{AB}
0.0201	0.0884	0.0264	0.551	0.0228	0.0987	0.0260	0.501
0.0267	0.117	0.0350	0.413	0.0368	0.159	0.0419	0.373
0.0357	0.157	0.0468	0.343	0.0449	0.194	0.0512	0.342
0.0506	0.222	0.0663	0.275	0.0607	0.263	0.0692	0.240
0.0605	0.266	0.0793	0.195	0.0764	0.331	0.0870	0.167
0.0727	0.320	0.0953	0.154	0.0845	0.366	0.0963	0.137
0.0851	0.374	0.112	0.119	0.0926	0.401	0.105	0.128
0.1015	0.446	0.133	0.098	0.1166	0.505	0.133	0.088
0.113	0.497	0.148	0.058	0.133	0.576	0.152	0.080
0.125	0.550	0.164	0.055	0.140	0.606	0.160	0.068

property of the turbulence in the thick axisymmetric stern boundary layer. The present set of experimental results is consistent with the conjecture of Townsend[15] that the flow patterns in a wake and in a boundary layer possess an overall structural similarity. It may not be necessary to use "local" equations for turbulent Reynolds stresses with a diffusion term and with a correction to the extra rate of strain.[9]

CONCLUSIONS

The present investigation of the thick axisymmetric turbulent boundary layer on an inflected stern without shoulder separation is an extension of the earlier research reported by Huang et al.[1,2] An additional comprehensive set of boundary layer measurements, including mean and turbulence velocity profiles, turbulence Reynolds stresses, static pressure distribution, and correlation length scales of the turbulence, are presented. The following major conclusions can be drawn.

The Preston[7] and Lighthill[8] displacement body concept has further been proven experimentally to be an efficient and accurate approach for computing the viscid and inviscid stern flow interaction on axisymmetric bodies. The measured static pressure distributions on the body and across the entire thick boundary layer were predicted by the displacement body method to an accuracy within one percent of dynamic pressure.

Neither the measured values of eddy viscosity nor the mixing length were found to be proportional to the local displacement thickness or the local boundary-layer thickness of the thick axisymmetric boundary layer. The measured mixing length of the thick axisymmetric stern boundary layer was again found to be proportional to the square root of the area of the turbulent annulus between the body surface and the edge of the boundary layer. This simple similarity hypothesis for the mixing length and the displacement body concept have been incorporated into the Douglas C-S differential boundary-layer method[5] by Wang and Huang.[3] The improved method predicts satisfactorily the measured mean velocity distributions in the entire stern boundary layer.

The measured correlation length scales of the turbulence and the measured Taylor microscales in the entire stern boundary layer are found to

be proportional to the square root of the annular area between the body surface and the edge of the turbulent boundary layer, which indeed is the appropriate overall length scale of the thick stern boundary layer.

ACKNOWLEDGMENT

The authors would like to thank the staff at the DTNSRDC Anechoic Flow Facility for their cooperation during the testing and to express their gratitude to John L. Leahy for his assistance with the instrumentation.

REFERENCES

1. Huang, T.T. et al., "Stern Boundary-Layer Flow on Axisymmetric Bodies," 12th Symposium on Naval Hydrodynamics, Washington, D.C. (5-9 Jun 1978). Available from National Academy of Sciences, Wash., D.C., pp. 127-147 (1979).

2. Huang, T.T. et al., "Propeller/Stern/Boundary-Layer Interaction on Axisymmetric Bodies: Theory and Experiment," DTNSRDC Report 76-0113 (1976).

3. Wang, H.T. and T.T. Huang, "Calculation of Potential Flow/ Boundary Layer Interaction on Axisymmetric Bodies," The ASME Symposium on Turbulent Boundary Layers, Niagara Falls, N.Y., pp. 47-57 (18-20 Jun 1979).

4. Hess, J.L. and A.M.O. Smith, "Calculation of Potential Flow About Arbitrary Bodies," Progress in Aeronautical Sciences, Vol. 8, Pergamon Press, New York, Chapter 1 (1966).

5. Cebeci, T. and A.M.O. Smith, Analysis of Turbulent Boundary Layers, Academic Press, New York (1974).

6. Granville, P.S., "The Calculation of the Viscous Drag of Bodies of Revolution," DTMB Report 849 (1953).

7. Preston, J.H., "The Effect of the Boundary Layer and Wake on the Flow Past a Symmetrical Aerofoil at Zero Incidence; Part I, The Velocity Distribution at the Edge of, and Outside the Boundary Layer and Wake," ARC R&M 2107 (1945).

8. Lighthill, M.J., "On Displacement Thickness," Journal of Fluid Mechanics, Vol. 4, Part 4, pp. 383-392 (1958).

9. Patel, V.C. and Y.T. Lee, "Thick Axisymmetric Boundary Layers and Wakes: Experiment and Theory," Paper 4, International Symposium on Ship Viscous Resistance, Göteborg, Sweden (1978).

10. McCarthy, J.H. et al., "The Roles of Transition, Laminar Separation, and Turbulence Stimulation in the Analysis of Axisymmetric Body Drag," 11th ONR Symposium on Naval Hydrodynamics, London (1976).

11. Huang, T.T. and C.H. von Kerczek, "Shear Stress and Pressure Distribution on a Surface Ship Model: Theory and Experiment," 9th ONR Symposium on Naval Hydrodynamics, Paris (1972). (Proceedings are available in U.S. Gov. Print. Office as ACR-203, Vol. 2.)

12. Dyne, G., "A Theoretical Scale Effect Study on the Propulsion Coefficient of a Body of Revolution," paper presented at Symposium on Hydrodynamics of Ship and Offshore Propulsion Systems, Sponsored: Det Norske Veritas, Høvik outside Oslo, Norway (20-25 Mar 1977).

13. Bradshaw, P. et al., "Calculation of Boundary Layer Development Using the Turbulent Energy Equation," Journal of Fluid Mechanics, Vol. 28 (1967).

14. Frenkiel, F.N. et al., "Grid Turbulence in Air and Water," The Physics of Fluids, Vol. 22, No. 9, pp. 1606-1617 (1979).

15. Townsend, A.A., "Flow Patterns of Large Eddies in a Wake and in a Boundary Layer," J. Fluid Mech., Vol. 95, Part 3, pp. 515-537 (1979).

INITIAL DISTRIBUTION

Copies	
1	WES
1	U.S. ARMY TRAS R&D Marine Trans Div
1	CHONR/438 Cooper
2	NRL 1 Code 2027 1 Code 2629
1	ONR/Boston
1	ONR/Chicago
1	ONR/New York
1	ONR/Pasadena
1	ONR/San Francisco
1	NORDA
3	USNA 1 Tech Lib 1 Nav Sys Eng Dept 1 B. Johnson
3	NAVPGSCOL 1 Lib 1 T. Sarpkaya 1 J. Miller
1	NADC
1	NOSC/Lib
1	NCSC/712, D. Humphreys
1	NCEL/Code 131
1	NSWC, White Oak/Lib
1	NSWC, Dahlgren/Lib
1	NUSC/Lib

Copies	
14	NAVSEA 1 SEA 033 1 SEA 03D 1 SEA 05T 1 SEA 05H 1 SEA 312 1 SEA 32 1 SEA 321 1 SEA 32R 1 SEA 521 1 SEA 524 1 SEA 62P 3 SEA 996
1	NAVFAC/Code 032C
1	NAVSHIPYD PTSMH/Lib
1	NAVSHIPYD PHILA/Lib
1	NAVSHIPYD NORVA/Lib
1	NAVSHIPYD CHASN/Lib
1	NAVSHIPYD LBEACH/Lib
2	NAVSHIPYD MARE 1 Lib 1 Code 250
1	NAVSHIPYD PUGET/Lib
1	NAVSHIPYD PEARL/Code 202.32
1	NAVSEC, NORVA/6660.03, Blount
12	DTIC
1	AFOSR/NAM
1	AFFOL/FYS, J. Olsen
2	MARAD 1 Div of Ship R&D 1 Lib
1	NASA/HQ/Lib

Copies	
1	NASA/Ames Res Ctr, Lib
2	NASA/Langley Res Ctr 1 Lib 1 D. Bushnell
3	NBS 1 Lib 1 P.S. Klebanoff 1 G. Kulin
1	NSF/Eng Lib
1	LC/Sci & Tech
1	DOT/Lib TAD-491.1
2	MMA 1 National Maritime Research Center 1 Lib
1	U. of Bridgeport/E. Uram
4	U. of Cal/Dept Naval Arch, Berkeley 1 Lib 1 W. Webster 1 J. Paulling 1 J. Wehausen
2	U. of Cal, San Diego 1 A.T. Ellis 1 Scripps Inst Lib
5	CIT 1 Aero Lib 1 T.Y. Wu 1 A.J. Acosta 1 I. Sabersky 1 D. Coles
1	City College, Wave Hill/ Pierson
1	Catholic U. of Amer./Civil & Mech Eng
1	Colorado State U./Eng Res Cen

Copies	
1	U. of Connecticut/Scottron
1	Cornell U./Shen
2	Florida Atlantic U. 1 Tech Lib 1 S. Dunne
2	Harvard U. 1 G. Carrier 1 Gordon McKay Lib
1	U. of Hawaii/Bretschneider
1	U. of Illinois/J. Robertson
4	U. of Iowa 1 Lib 1 L. Landweber 1 J. Kennedy 1 V.C. Patel
3	Johns Hopkins U. 1 O. Phillips 1 S. Corrsin 1 R. Long
1	Kansas State U./Nesmith
1	U. of Kansas/Civil Eng Lib
1	Lehigh U./Fritz Eng Lab Lib
6	MIT 1 Lib 1 P. Mandel 1 J.R. Kerwin 1 P. Leehey 1 M. Abkowitz 1 J.N. Newman
4	U. of Minn/St. Anthony Falls 1 Silberman 1 Lib 1 Song 1 R. Arndt

Copies	
4	U. of Mich/NAME 1 Lib 1 F. Ogilivie 1 Hammitt 1 Cough
2	U. of Notre Dame 1 Eng Lib 1 Strandhagen
2	New York U./Courant Inst 1 A. Peters 1 J. Stoker
3	Penn State 1 B.R. Parkin 1 R.E. Henderson 1 ARL Lib
1	Princeton U./Mellor
2	U. of Rhode Island 1 F.M. White 1 T. Kowalski
1	Science Application, Inc. McLean, VA C. Von Kerczek
5	SIT 1 Lib 1 Breslin 1 Savitsky 1 P.W. Brown 1 Tsakonas
1	U. of Texas/Arl Lib
1	Utah State U./Jeppson
2	Southwest Res Inst 1 Applied Mech Rev 1 Abramson
3	Stanford U. 1 Eng Lib 1 R. Street, Dept Civil Eng 1 S.J. Kline, Dept Mech Eng

Copies	
1	Stanford Res Inst/Lib
1	U. of Virginia/Aero Eng Dept
1	U. of Washington/Arl Tech Lib
3	VPI 1 H.L. Moses, Dept Mech Eng 1 D.P. Telionis, Dept Mech Eng 1 J. Schetz, Dept Aero & Ocean Eng
3	Webb Inst 1 Library 1 Lewis 1 Ward
1	Woods Hole/Ocean Eng
1	Worchester PI/Tech Lib
1	SNAME/Tech Lib
1	Bell Aerospace
1	Bethlehem Steel/Sparrows Point
1	Bethlehem Steel/New York/Lib
2	Boeing Company/Seattle 1 Marine System 1 P. Rubbert
1	Bolt, Beranek & Newman/Lib
1	Exxon, NY/Design Div Tank Dept
1	Exxon Math & System, Inc.
1	General Dynamics, EB/ Boatwright
1	Flow Research
1	Gibbs & Cox/Tech Info

Copies	
1	Grumman Aerospace Corp/Lib
5	Hydronautics 1 Lib 1 E. Miller 1 V. Johnson 1 C.C. Hsu 1 M. Tulin
1	Lockheed, Sunnyvale/Waid
1	Lockheed, California/Lib
1	Lockheed, Georgia/Lib
2	McDonnell Douglas, Long Beach 1 T. Cebeci 1 J. Hess
1	Newport News Shipbuilding/ Lib
1	Nielsen Eng & Res
1	Northrop Corp/Aircraft Div.
3	Rand Corp 1 E.R. Van Driest 1 C. Gazley 1 J. Aroesty
1	Rockwell International/B. Ujihara
1	Sperry Rand/Tech Lib
1	Sun Shipbuilding/Chief Naval Arch
1	Robert Taggart
1	TRW Systems Group/Lib
1	Tracor
1	United Technology/East Hartford, Conn.
2	Westinghouse Electric 1 M.S. Macovsky 1 Gulino

CENTER DISTRIBUTION

Copies	Code	Name
1	1500	W.B. Morgan
1	1504	V.J. Monacella
1	1507	D.S. Cieslowski
1	1508	R.S. Rothblum
1	1521	P. Pien
1	1524	Y.T. Shen
1	1524	W.C. Lin
1	1524	W. Day
1	1532	G. Dobay
1	1532	M. Wilson
1	1541	P. Granville
1	1542	B. Yim
1	1544	R. Cumming
1	1544	R. Boswell
1	1544	E. Caster
1	1544	S. Jessup
1	1544	K.F. Lin
30	1552	T.T. Huang
1	1552	N.C. Groves
1	1552	G.S. Belt
1	1552	H.T. Wang
1	1552	J. McCarthy
1	1552	T. Langan
1	1555	M.S. Chang
1	1560	G. Hagen
1	1561	C.M. Lee
1	1562	M. Martin
1	1564	J. Feldman
1	1568	G. Cox
1	1572	M.D. Ochi
1	1572	E. Zarnick
1	1576	W.E. Smith

Copies	Code	Name
1	1606	T.C. Tai
1	1615	R.J. Furey
1	1802.1	H. Lugt
1	1802.2	F. Frenkiel
1	1840	J. Schot
1	1843	H. Haussling
1	19	M.M. Sevik
1	1940	J.T. Shen
1	1942	B.E. Bowers
1	1942	T.M. Farabee
1	1942	F.E. Geib
1	1942	T.C. Mathews
1	1946	J.A. Padgett
10	5211.1	Reports Distribution
1	522.1	Unclassified Lib (C)
1	522.2	Unclassified Lib (A)